Impact of the surface energy coefficient on the deformation properties of atomic nuclei as predicted by Skyrme energy density functionals

W. Ryssens,[1] M. Bender,[1] K. Bennaceur,[1,2] P.-H. Heenen,[3] and J. Meyer[1]
[1]*IPNL, Université de Lyon, Université Lyon 1, CNRS/IN2P3, F-69622 Villeurbanne, France*
[2]*Department of Physics, University of Jyväskylä, PO Box 35 (YFL), FI-40014, Finland*
[3]*PNTPM, CP229, Université Libre de Bruxelles, B-1050 Bruxelles, Belgium*

(Received 9 September 2018; revised manuscript received 15 November 2018; published 25 April 2019)

Background: In the framework of nuclear energy density functional (EDF) methods, many nuclear phenomena are related to the deformation of intrinsic states. Their accurate modeling relies on the correct description of the change of nuclear binding energy with deformation. The two most important contributions to the deformation energy have their origin in shell effects that are correlated to the spectrum of single-particle states, and the deformability of nuclear matter, that can be characterized by a model-dependent surface energy coefficient a_{surf}.
Purpose: With the goal of improving the global performance of nuclear EDFs through the fine-tuning of their deformation properties, the purpose of this study is threefold. First, to analyze the impact of systematic variations of a_{surf} on properties of nuclei; second, to identify observables that can be safely used to narrow down the range of appropriate values of a_{surf} to be targeted in future parameter fits; third, to analyze the interdependence of a_{surf} with other properties of a nuclear EDF.
Methods: Results for a large variety of relevant observables of deformed nuclei obtained from self-consistent mean-field calculations with a set of purpose-built SLy5sX parametrizations of the Skyrme EDF are correlated with the value of a_{surf}.
Results: The performance of the SLy5sX parametrizations for characteristic energies of the fission barriers of ^{180}Hg, ^{226}Ra, and ^{240}Pu, excitation energies, electromagnetic moments and moments of inertia of superdeformed states in the $A \approx 190$ region, properties of shape coexisting states at normal deformation in the Pb, Kr, and Zr region, properties of octupole-deformed ^{144}Ba, even-even Th isotopes, and ^{110}Zr, separation energies along isotopic and isotonic chains are compared with available experimental data.
Conclusions: The three main conclusions are that there is an evident preference for a comparatively low value of a_{surf}, as expected from the performance of existing parametrizations; that the isospin dependence of the surface energy also needs further fine-tuning in order to describe trends across the chart of nuclei; and that a satisfying simultaneous description of fission barriers and superdeformed states requires a better description of the single-particle spectra.

DOI: 10.1103/PhysRevC.99.044315

I. INTRODUCTION

Self-consistent mean-field models based on energy density functionals (EDFs) [1] are among the tools of choice to study nuclear structure across the entirety of the nuclear chart. Many different types of EDFs are used that are either nonrelativistic or relativistic, use contact terms with gradients or have finite-range terms of various kinds, and use different types of density dependencies. Because of its flexibility and computational simplicity, however, the local nonrelativistic Skyrme EDF is arguably the most widely used form for such calculations. Marrying a microscopic description of the nucleus with a modest computational cost, all types of EDFs allow for the description of many properties of nuclei, from the properties of infinite nuclear matter to those of the ground states of finite nuclei such as their binding energy, shell structure, radii, and other characteristics of their density distribution, to more subtle characteristics of excited states such as shape coexistence and various types of rotational bands, to their response properties, fission barriers, and behavior in low-energy nuclear reactions.

In one way or the other, almost all of these nuclear structure phenomena are associated with deformed intrinsic shapes of the nucleus. In the simple picture of the nucleus as a liquid drop, however, the ground states of all nuclei up to charge numbers Z of about 100 are spherical. Indeed, within that framework the deformation of the nuclear shape leads to a decrease in total binding energy that is mainly determined by the interplay between two contributions that overall reduce the total binding energy: On the one hand, the surface energy grows with deformation—as it increases the size of the nuclear surface—while on the other hand the Coulomb energy decreases with deformation, as the average distance between protons, which repel each other, becomes larger. In light systems the competition of these two terms is dominated by the surface energy, but with increasing Z the Coulomb energy is taking over until for $Z \simeq 100$ it decreases quicker with deformation than the surface energy increases. As a result, the

spherical shape becomes a maximum of the energy landscape which is monotonically falling off until the nucleus splits into two or even more fragments. In this picture, deformed states of nuclei are generated by shell effects that give an additional contribution to the binding energy. Its quick variation with deformation generates local minima and barriers on top of the smooth surface from the liquid-drop energy [2,3]. As has been demonstrated already a long time ago [4,5], the results of nuclear self-consistent EDF calculations can be interpreted with the same vocabulary of macroscopic liquid-drop and microscopic shell-correction energy, although neither of the two is actually calculated as an ingredient of the model.

It is well known that the dominant contribution to the surface energy $E_{\rm surf}$ of a spherical nucleus simply scales with $A^{2/3}$. In the liquid-drop model (LDM), the proportionality factor between the two is called the surface energy coefficient $a_{\rm surf}$. Like the volume energy, the surface energy depends on the asymmetry between proton and neutron number, which is parametrized through a surface symmetry energy with corresponding coefficient $a_{\rm ssym}$. Realistic finite nuclei, however, are too small to unambiguously separate the surface energy and its isospin dependence from higher-order and pairing contributions to the total liquid-drop binding energy [6–8], which compromises their determination from experimental data for binding energies. These coefficients, however, can also be used to characterize nuclear EDFs. Their values can for example be calculated for the idealized model system of semi-infinite nuclear matter. The precise value of $E_{\rm surf}$ obtained from such calculation nonetheless still depends on choices made for details of the modeling; see Refs. [8,9] and references therein. As a consequence, it appears to be impossible to establish unique model-independent empirical values for $a_{\rm surf}$ and $a_{\rm ssym}$.

While there is an obvious correlation between the values of $a_{\rm surf}$ and $a_{\rm ssym}$ of a nuclear EDF and the systematics of calculated deformation properties [10–13], its analysis is often compromised by the use of parametrizations that have been adjusted with different protocols such that the parametrizations differ in many respects, not just the surface properties. The recent series of eight parametrizations of the standard Skyrme EDF, SLy5s1–SLy5s8 [8,9] with their systematically varied $a_{\rm surf}$ offer the possibility for a much cleaner separation of the surface energy from other contributions.

The fit of the SLy5sX parametrizations is part of the ongoing efforts to improve the descriptive power of nuclear energy density functionals, and which concern both their functional form and the procedure used to adjust their parameters. Important recent milestones for the latter concern strategies to avoid unphysical finite-size instabilities [14] and the quantification of correlations between model parameters and data, that also allows for estimating the statistical errors of observables related to the fit protocol [7,15–17].

The construction of the SLy5sX parametrizations is the first step towards establishing a protocol to better constrain the deformation properties of heavy nuclei such as fission barriers during the parameter adjustment in a computationally efficient way. To that end, the isoscalar surface energy coefficient has been varied in small equidistant steps in the region where it can be expected to find a realistic value. Indeed, there is no possibility to establish a unique model-independent empirical value for $a_{\rm surf}$ that can be determined *a priori*. Hence, one has to choose a scheme for its calculation, carry out a series of fits that cover the relevant region and determine the value that corresponds to a realistic description of nuclei *a posteriori*. If necessary, this value can be fed back into a series of refits covering its vicinity until a best fit is achieved iteratively. The fine-tuning of the D1S parametrization of the Gogny interaction to fission properties was in fact based on similar ideas [18].

Other previous attempts to fine-tune deformation properties during an EDF's parameter fit either relied on semiclassical estimates for the fission barrier height, as done for SkM* in Ref. [10], or on the adjustment of the excitation energy of the fission isomer in the actinide region as done for UNEDF1 and UNEDF2 in Refs. [16,17].

Using the SLy5sX parametrizations as the starting point, the goal of the present article is threefold.

(i) First, we want to benchmark the descriptive power of the series of SLy5sX parametrizations on typical properties of nuclei, scrutinizing their differences in dependence of their value for $a_{\rm surf}$ for typical observables of deformed nuclei frequently calculated with nuclear EDF methods.

(ii) Second, we want to identify observables that are directly affected by a change in $a_{\rm surf}$ and which can then in the future be used for the adjustment of a "best value" for $a_{\rm surf}$ during a parameter fit aiming at a unique best fit of an EDF.

(iii) Third, we want to analyze to which extent a constraint on $a_{\rm surf}$ is independent from other data, be they used during the fit or not. As many terms in the EDF contribute to it, there is the possibility that setting $a_{\rm surf}$ to some specific value substantially degrades other properties of the parametrizations that are less strictly constrained.

This paper is organized as follows: Section II provides a discussion of the nuclear matter properties of the SLy5sX parametrizations of the Skyrme EDF. Section III discusses the mapping of EDF results on a liquid-drop model, which will be used as a diagnostic tool later on. Section IV analyzes the differences of results obtained with the set of SLy5sX parametrizations for fission barriers of selected representative heavy and superheavy nuclei, superdeformed states in the $A \approx 190$ mass region, shape coexisting states at normal deformation for the example of ^{186}Pb, ^{74}Kr, and ^{110}Zr, and some selected octupole-deformed ground states. Finally, in Sec. V we summarize the main results of the paper and we outline new constraints for the construction of EDFs.

II. SLy5sX PARAMETRIZATIONS

A. Energy density functional

In the context of the Skyrme EDF method, it is customary to split the energy density functional into five terms [1]:

$$E_{\rm tot} = E_{\rm kin} + E_{\rm Skyrme} + E_{\rm Coul} + E_{\rm pair} + E_{\rm corr}, \qquad (1)$$

which correspond to the kinetic energy, the actual Skyrme EDF that models of the strong interaction between the nucleons in the particle-hole channel, the Coulomb energy resulting from the electromagnetic repulsion between protons, a pairing EDF modeling the strong-interaction in the particle-particle channel, and correction terms for spurious zero-point motion that result from the mean-field approximation.

The SLy5sX parametrizations considered throughout this article use the standard form of the Skyrme EDF combining central and spin-orbit terms up to next-to-leading order in derivatives with a simple density dependence of the gradientless terms. As for SLy5 [19], the contribution of the central interaction to the tensor terms that are bilinear in spin-current tensor density $J_{\mu\nu}(\mathbf{r})$ is kept, while the correction terms for spurious zero-point motion are limited to the one-body contribution to the center-of-mass correction $E_{\rm cm}$. No additional independent tensor force is taken into account when generating the EDF. Also, like for SLy5, the direct Coulomb term is calculated from the point-proton density, while the Coulomb exchange term is approximated by the local Slater approximation.

For time-reversal-invariant systems, the Skyrme EDF then takes the form

$$\begin{aligned} E_{\rm Skyrme}^{\rm even} &= E_{\rho^2} + E_{\rho^{2+\alpha}} + E_{\rho\tau} + E_{\rho\Delta\rho} + E_{\rho\nabla J} + E_{JJ} \\ &= \sum_{t=0,1} \int d^3r \Big[C_t^{\rho\rho}\, \rho_t^2(\mathbf{r}) + C_t^{\rho\rho\rho^\alpha}\, \rho_0^\alpha(\mathbf{r})\, \rho_t^2(\mathbf{r}) \\ &\quad + C_t^{\rho\tau}\, \rho_t(\mathbf{r})\, \tau_t(\mathbf{r}) + C_t^{\rho\Delta\rho}\, \rho_t(\mathbf{r})\, \Delta\rho_t(\mathbf{r}) \\ &\quad + C_t^{\rho\nabla\cdot J}\, \rho_t(\mathbf{r})\, \nabla\cdot\mathbf{J}_t(\mathbf{r}) \\ &\quad - C_t^{sT} \sum_{\mu,\nu} J_{t,\mu\nu}(\mathbf{r})\, J_{t,\mu\nu}(\mathbf{r}) \Big]. \end{aligned} \tag{2}$$

It is a functional of the isoscalar ($t = 0$) and isovector ($t = 1$) local density $\rho_t(\mathbf{r})$, kinetic density $\tau_t(\mathbf{r})$, and spin-current tensor density $J_{t,\mu\nu}(\mathbf{r})$. The latter has nine independent Cartesian components labeled by μ and ν, with the spin-orbit current $\mathbf{J}_t(\mathbf{r})$ being its rank-1 contraction. The C coefficients are the coupling constants of the various terms in the isoscalar ($t = 0$) and isovector ($t = 1$) channels. For further details and the definition of these quantities, see Refs. [20–22].

All densities entering Eq. (2) are even under time reversal. For the calculation of the rotational bands discussed in Sec. IV E, where time-reversal invariance is broken, additional terms have to be considered that depend on the time-odd spin density $\mathbf{s}_t(\mathbf{r})$, current density $\mathbf{j}_t(\mathbf{r})$, and kinetic spin density $\mathbf{T}_t(\mathbf{r})$ [21],

$$\begin{aligned} E_{\rm Skyrme}^{\rm odd} &= \sum_{t=0,1} \int d^3r \Big[C_t^{ss}\, \mathbf{s}_t^2(\mathbf{r}) + C_t^{ss\rho^\alpha}\, \rho_0^\alpha(\mathbf{r})\, \mathbf{s}_t^2(\mathbf{r}) \\ &\quad + C_t^{sT}\, \mathbf{s}_t(\mathbf{r})\cdot\mathbf{T}_t(\mathbf{r}) + C^{s\Delta\mathbf{s}}\, \mathbf{s}_t(\mathbf{r})\cdot\Delta\mathbf{s}_t(\mathbf{r}) \\ &\quad - C_t^{\rho\tau}\, \mathbf{j}_t^2(\mathbf{r}) + C_t^{\rho\nabla J}\, \mathbf{s}_t(\mathbf{r})\cdot\nabla\times\mathbf{j}_t(\mathbf{r}) \Big]. \end{aligned} \tag{3}$$

This part of the EDF is colloquially called the "time-odd" part of the functional. Although constructed out of time-odd densities, the EDF itself is time-even. Note that some of the coupling constants in the time-even (2) and time-odd (3) parts are necessarily equal, up to a sign, for reasons of Galilean invariance [23]. The coupling constants of the other terms in the time-odd part of the EDF can be linked to those of the time-even part (2) by calculating the entire Skyrme EDF as the expectation value of a density-dependent zero-range two-body interaction for a Slater determinant [21,23]. This, however, is not always done, in particular because the term containing the Laplacian of the spin density $\Delta\mathbf{s}_t(\mathbf{r})$ can be the source of a nonphysical finite-size instability in the spin channels [21,24–26] when keeping its coupling constant at the Skyrme-force value. Adding the constraint proposed in Ref. [14] to the fit protocol, it has been ensured that the SLy5sX parametrizations are free of such instabilities for values of the densities encountered in finite nuclei.

The SLy5sX parametrizations were adjusted to properties of doubly magic nuclei for which pairing correlations vanish at the mean-field level. The calculations that are presented here require the introduction of pairing correlations, which is done by solving the HFB equations with the two-basis method [27]. We use a simple pairing EDF of the form

$$\mathcal{E}_{\rm pairing} = \sum_{q=p,n} \frac{V_q}{4} \int d^3r \left[1 - \frac{\rho_0(\mathbf{r})}{\rho_c} \right] \tilde{\rho}_q^*(\mathbf{r})\, \tilde{\rho}_q(\mathbf{r}), \tag{4}$$

where the $\tilde{\rho}_q(\mathbf{r})$ are local pairing densities that become complex when time-reversal symmetry is broken. As all SLy5sX parametrizations have almost the same effective mass as the SLy4 parametrization, we have taken the same values $V_q = -1250$ MeV fm^{-3} and $\rho_q = 0.16$ fm^{-3}, originally adjusted to moments of inertia of superdeformed rotational bands in the $A \approx 190$ region [28], as done in many previous studies using SLy4. A smooth cutoff above and below the Fermi energy is introduced by multiplying the contribution from the single-particle state with index k by the factor

$$f_k = [1 + e^{(\epsilon'_k - \Delta\epsilon_q)/\mu_q}]^{-1/2} [1 + e^{(\epsilon'_k + \Delta\epsilon_q)/\mu_q}]^{-1/2}, \tag{5}$$

when summing the pair densities in the basis that diagonalizes the single-particle Hamiltonian $\hat{h}$. The cutoff depends on the distance $\epsilon'_k \equiv \epsilon_k - \lambda_q$ of a given eigenvalue ϵ_k of $\hat{h}$ from the Fermi energy λ_q of the nucleon species q. For the parameters, we choose $\mu_q = 0.5$ MeV, and $\Delta\epsilon_q = 5.0$ MeV for both protons and neutrons as done in the past [28].

Finally, unless explicitly mentioned otherwise, we have employed the Lipkin-Nogami prescription as in Ref. [28] in order to avoid a collapse of pairing correlations.

B. Global properties of the SLy5sX parametrizations

The SLy5sX parametrizations were adjusted with an auxiliary condition on their surface energy coefficient in such a way that it takes a different value for each of them. The fit protocol used for their adjustment [8] is an update of the Saclay-Lyon protocol originally set up in the 1990s [19]. The most noteworthy differences to Ref. [19] are the additional constraint proposed in Ref. [14] that prevents the often encountered appearance of unphysical finite-size instabilities in the spin-channels already mentioned above, and an additional constraint on the slope of the symmetry energy that will be commented on below.

TABLE I. Properties of infinite nuclear matter as obtained with the SLy5sX parametrizations: saturation density $\rho_{\rm sat}$ in fm^{-3}, energy per particle $E/A = a_{\rm vol}$ in MeV, incompressibility K_∞ in MeV, isoscalar effective mass m_0^*/m, symmetry energy coefficient $J = a_{\rm sym}$ and its slope L in MeV, and enhancement factor of the Thomas-Reiche-Kuhn sum rule κ_v.

	$\rho_{\rm sat}$	E/A	K_∞	m_0^*/m	J	L	κ_v
SLy5s1	0.1598	−15.772	222.1	0.7392	31.43	48.1	0.3047
SLy5s2	0.1603	−15.818	223.2	0.7350	31.60	48.3	0.3063
SLy5s3	0.1607	−15.864	224.3	0.7309	31.77	48.4	0.3082
SLy5s4	0.1612	−15.911	225.4	0.7273	31.94	48.5	0.3105
SLy5s5	0.1618	−15.958	226.4	0.7243	32.11	48.6	0.3131
SLy5s6	0.1623	−16.005	227.3	0.7217	32.29	48.8	0.3160
SLy5s7	0.1629	−16.053	228.3	0.7196	32.46	48.9	0.3191
SLy5s8	0.1634	−16.101	229.1	0.7178	32.64	49.0	0.3225

Tables I and II list the most relevant properties of the SLy5sX parametrizations for the model systems of infinite (INM) and semi-infinite (SINM) nuclear matter, respectively. While the properties of INM listed in Table I can be obtained from simple functions of the parameters, the properties of SINM have to be deduced from a numerical calculation of this system. The latter can be carried out in different frameworks, each of which yields slightly different values, which is the reason why Table II lists values for $a_{\rm surf}$ calculated from quantal Hartree-Fock (HF) as well as semiclassical Extended Thomas-Fermi (ETF) and Modified Thomas-Fermi (MTF) calculations [8,9]. While values for $a_{\rm surf}$ obtained with different models for SINM are visibly different for a given parametrization, the difference between values of different parametrizations obtained within the same model for SINM is almost independent of the choice of model [8]. We also list values for the surface symmetry energy coefficient $a_{\rm ssym}$, but only from HF calculations. Establishing a value for $a_{\rm ssym}$ turns out to be even more delicate than determining $a_{\rm surf}$. The generalization of MTF to asymmetric SINM is not straightforward and requires further approximations, and there are several possibilities for the protocol to extract $a_{\rm ssym}$ from a series of SINM calculations with varying asymmetry. A detailed analysis of the model dependence of the resulting $a_{\rm ssym}$ from such calculations will be presented elsewhere [29].

TABLE II. Properties of semi-infinite nuclear matter as obtained with the SLy5sX parametrizations: Surface energy coefficient $a_{\rm surf}$ as obtained within the HF, ETF, and MTF approaches and surface symmetry energy coefficient $a_{\rm ssym}$ as obtained within the HF method, all in MeV. The last column lists the isoscalar coupling constant $C_0^{\nabla\cdot J} = 3C_1^{\nabla\cdot J}$ of the spin-orbit term in the EDF (2) in MeV fm^{-5}.

	$a_{\rm surf}^{\rm (MTF)}$	$a_{\rm surf}^{\rm (ETF)}$	$a_{\rm surf}^{\rm (HF)}$	$a_{\rm ssym}^{\rm (HF)}$	$C_0^{\rho\nabla\cdot J}$
SLy5s1	18.00	17.15	17.55	−48.09	−86.61
SLy5s2	18.20	17.34	17.74	−48.21	−85.71
SLy5s3	18.40	17.53	17.93	−48.56	−84.65
SLy5s4	18.60	17.73	18.12	−49.01	−83.50
SLy5s5	18.80	17.92	18.31	−49.73	−82.31
SLy5s6	19.00	18.11	18.50	−50.53	−81.08
SLy5s7	19.20	18.31	18.70	−51.58	−79.82
SLy5s8	19.40	18.50	18.89	−52.70	−78.54

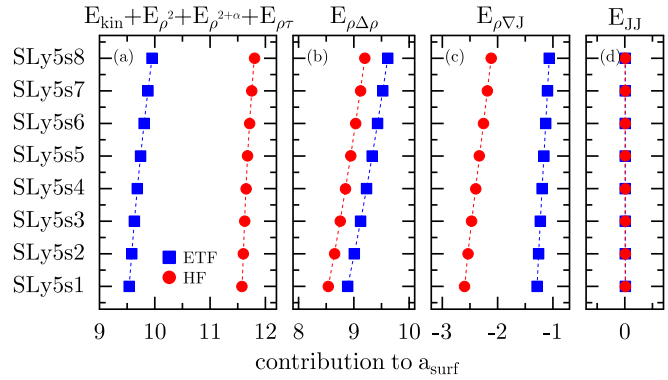

FIG. 1. Decomposition of the surface energy coefficient in the contributions from terms in the EDF that contribute to INM (a), gradient terms (b), spin-orbit terms (c), and tensor terms (d). All panels share the same energy scale.

The SLy5sX parametrizations were adjusted with a constraint on the MTF value of $a_{\rm surf}$, which is the most computationally friendly approach for its calculation. Going from SLy5s1 with the lowest $a_{\rm surf}^{\rm MTF} = 18.0$ MeV to SLy5s8 with the highest value of 19.4 MeV in equal steps of 0.2 MeV covers the range typically found for widely used Skyrme parametrizations [8].

Because of the limited number of degrees of freedom of the Skyrme EDF, the value of $a_{\rm surf}$ cannot be varied independently from the other nuclear matter properties. As with $a_{\rm surf}$ one property is constrained to a precise value, the others readjust themselves. As can be seen from Table I, the properties of INM vary slowly and systematically as a function of $a_{\rm surf}$. In fact, all nuclear matter properties listed in Table I have been constrained in one way or the other during the parameter fit. Keeping the values for $\rho_{\rm sat}$, $E/A = a_{\rm vol}$, K_∞, $J = a_{\rm sym}$, m_0^*/m, and κ_v near the empirical ones has already been proposed in the original fit protocol of [19]. The slope of the symmetry energy L, which is not well fixed by data on finite nuclei, was not constrained in the protocol of Ref. [19]. During the parameter fit of the SLy5sX, however, the value of L started to change on a large scale when varying $a_{\rm surf}$, such that it has been constrained to the interval of (50 ± 2) MeV in order to keep bulk properties at similar values [8]. The variation of these nuclear matter properties when going from one SLy5sX parametrization to another can be expected to have some impact on the properties of finite nuclei.

The value for $a_{\rm surf}$ is determined by all isoscalar terms in the time-even part of the Skyrme EDF, Eq. (2), as well as the kinetic energy $E_{\rm kin}$ in Eq. (1). Figure 1 shows the decomposition of $a_{\rm surf}$ into terms that contribute to E/A of INM ($E_{\rm kin} + E_{\rho^2} + E_{\rho^{2+\alpha}} + E_{\rho\tau}$), gradient terms in the density ($E_{\rho\Delta\rho}$), spin-orbit terms ($E_{\rho\nabla J}$) and tensor terms (E_{JJ}). Results are shown for calculations performed within the semiclassical ETF and the microscopic HF method. For the MTF method, which because of its numerical efficiency was the tool of choice to constrain the $a_{\rm surf}$ of the SLy5sX parametrizations during their fit [8], such decomposition cannot be made.

There are obvious differences between the decompositions of $a_{\rm surf}$ when it is calculated with either the HF or ETF method. We focus, however, on the decomposition of the ETF result first. In this case, the INM and gradient terms are of comparable size and clearly dominate, while the spin-orbit term $E_{\rho\nabla J}$ brings a small, but non-negligible, correction of opposite sign. For the SLy5sX parametrizations that only have a contribution from the central force to E_{JJ}, but no explicit tensor interaction, with about 10 keV this term's contribution to $a_{\rm surf}$ is so small that it cannot be resolved in the figure. All terms contribute coherently to the increase in surface energy when going from SLy5s1 to SLy5s8, with changes in the gradient and spin-orbit terms being larger than those of the INM terms.

When calculated in HF, however, the contribution from INM terms is about 2 MeV larger than for ETF, whereas the gradient and spin-orbit terms are smaller, leading to the net difference of about 0.4 MeV between $a_{\rm surf}^{\rm (HF)}$ and $a_{\rm surf}^{\rm (ETF)}$ reported in Table II. The slopes of the INM and spin-orbit terms are also different when calculated in HF or ETF, but in the opposite direction such that the slope of their sums is almost identical for both methods as already pointed out in Ref. [8]. The variational calculation of the binding energy of SINM ensures that the total energy obtained in the quite different variational spaces of the HF and ETF methods are close, but does not guarantee that the individual contributions have the same size. We also recall that $a_{\rm surf}$ is obtained as the difference between two large numbers that typically are two orders of magnitude larger, which tends to further amplify the differences between the methods.

The change of the contribution of the INM terms to $a_{\rm surf}$ when going from SLy5s1 to SLy5s8 is reflected by the systematic changes of INM parameters listed in Table II. INM and SINM parameters are clearly intertwined in a self-consistent model, and as long as the parameters of $E_{\rho^2}+E_{\rho^{2+\alpha}}+E_{\rho\tau}$ are not kept fixed, the fit protocol shuffles contributions between them in order to optimize the penalty function. Only about half of the change of $a_{\rm surf}$ when going from SLy5s1 to SLy5s8 originates in the coupling constants of the gradient term $E_{\rho\Delta\rho}$. The contribution of the spin-orbit term to $a_{\rm surf}$ also varies slowly, meaning that the present fit protocol interweaves the "macroscopic" and "microscopic" aspects of a parametrization: SLy5s1 with its smallest $a_{\rm surf}$ produces spin-orbit splittings that are about 10% larger than those from SLy5s8, which has the largest $a_{\rm surf}$ in the series. As is discussed below, this sometimes compromises the possibility to distinguish the change in surface energy from changes in shell effects when comparing parametrizations.

III. LIQUID-DROP MODEL ESTIMATES OF SURFACE ENERGY

Below, we compare the results from self-consistent calculations with estimates of total and deformation energies obtained from a LDM whose parameters are extracted from the nuclear matter properties of the same effective interaction.

For spherical nuclei, we use the following form of the LDM energy, that is composed of volume, volume symmetry, surface, and surface symmetry energies as well as direct and exchange Coulomb terms,

$$E_{\rm LDM}(N,Z) = (a_{\rm vol}+a_{\rm sym}\,I^2)A + (a_{\rm surf}+a_{\rm ssym}\,I^2)A^{2/3} + \frac{3}{5}\frac{e^2}{r_0}\frac{Z^2}{A^{1/3}} - \frac{3}{4}\frac{e^2}{r_0}\left(\frac{3}{2\pi}\right)^{2/3}\frac{Z^{4/3}}{A^{1/3}}, \quad (6)$$

where $A=N+Z$ and $I=\frac{N-Z}{N+Z}$. The volume ($a_{\rm vol}$) and volume symmetry ($a_{\rm sym}$) energy coefficients can be related to properties of INM at the saturation point, whereas the surface ($a_{\rm surf}$) and surface symmetry ($a_{\rm ssym}$) energy coefficients are connected to properties of SINM. The radius constant r_0 entering the Coulomb energies is determined by the nuclear matter saturation density $\rho_{\rm sat}$ through the relation $r_0^3=3/(4\pi\rho_{\rm sat})$. The faithful reproduction of binding energies from self-consistent calculations would require additional higher-order terms [6,7], but this is irrelevant for the purpose of our further discussion. We also omit the usual pairing term in Eq. (6), as its parameters are mainly determined by the pairing energy functional (4).

In general, the surface symmetry energy coefficient $a_{\rm ssym}$ has the opposite sign of the surface energy coefficient $a_{\rm surf}$, which naturally follows from the volume and volume symmetry energy coefficients also having the opposite sign.

For the following discussion it is useful to define an asymmetry-dependent *effective* surface energy coefficient

$$a_{\rm surf,eff}(N,Z) \equiv a_{\rm surf} + a_{\rm ssym}\,I^2. \quad (7)$$

As the value of the $a_{\rm ssym}$ varies only very little among the SLy5sX parametrizations, cf. Table II, for a given nucleus the difference between $a_{\rm surf,eff}$ values of two parameterizations remains very close to the difference between their $a_{\rm surf}$ values. For ^{240}Pu, $a_{\rm surf,eff}$ from HF calculations of SINM takes the values of 15.29 and 16.42 MeV for SLy5s1 and SLy5s8, respectively. With 1.28 MeV, the difference between these values differs only little from the 1.34 MeV difference between the non-corrected values for $a_{\rm surf}$. By contrast, for a given parametrization $a_{\rm surf,eff}$ can take visibly different values for different nuclei: with 16.96 and 18.24 MeV for SLy5s1 and SLy5s8, respectively, $a_{\rm surf,eff}$ is 1.7 MeV larger for the neutron-deficient ^{180}Hg than for ^{240}Pu. From this follows immediately that the LDM fission barriers tend to decrease with asymmetry.

Mapping a self-consistent model on Eq. (6) is, however, nontrivial. The volume and volume symmetry energy coefficients, $a_{\rm vol}$ and $a_{\rm sym}$, respectively, are directly given by the INM properties E/A and J listed in Table I. However, as already mentioned, determining $a_{\rm surf}$ of an effective interaction has an inherent model dependence.

The deformation dependence of the LDM energy (6) is carried by the Coulomb and surface energies. The latter can be parametrized by multiplying the surface energy of the LDM formula (6) with a shape-dependent factor B_s [30] that is defined as the ratio between the area of the surface of a deformed liquid drop and a spherical one,

$$E_{\rm LDM}^{\rm surf}(N,Z,{\rm shape}) = (a_{\rm surf}+a_{\rm ssym}I^2)A^{2/3}\,B_s({\rm shape}). \quad (8)$$

Because of volume conservation of the nuclear liquid drop, this geometrical surface always grows with deformation. The direct Coulomb energy of a deformed liquid drop with sharp surface can in principle be parametrized through a similar factor $E^{\rm C}_{\rm LDM}(N, Z, \text{shape}) = a_c\, Z^2\, A^{-1/3}\, B_c(\text{shape})$ that has, however, a different deformation dependence [30]. In the analysis of deformation energy of finite nuclei in self-consistent calculations that is presented below, we replace only the sum $E_{\rm kin} + E_{\rm Skyrme} + E_{\rm corr}$ by a LDM estimate, while keeping $E_{\rm Coul}$ from the self-consistent model.

For arbitrary parametrizations of the nuclear shape, the size of B_s has in general to be determined through numerical integration of the surface area. Similarly, the multipole moments of an arbitrarily deformed liquid drop have in general also to be calculated through numerical integration. For some specific shape parametrizations, however, both can be developed in terms of a power series in the shape parameters [30]. This can then be used to estimate the change of macroscopic energy [30],

$$E_{\rm def} = E_{\rm surf} - E^{\rm sphere}_{\rm surf} + E_{\rm Coul} - E^{\rm sphere}_{\rm Coul}, \tag{9}$$

where the superscript "sphere" indicates the reference value of each term for a spherical shape.

A widely used parametrization of the nuclear surface for which such analytical expressions exist is its expansion in spherical harmonics,

$$R(\theta) = [c(\alpha)]^{-1}\, R_0 \left[1 + \sum_{\ell,m} \alpha_{\ell m} Y_{\ell m}(\theta)\right], \tag{10}$$

where $c(\alpha)$ is a normalization coefficient that ensures volume conservation. Limiting ourselves to axially symmetric ($\alpha_{\ell m} = 0$ for $m \neq 0$) and reflection-symmetric ($\alpha_{\ell m} = 0$ for odd ℓ) shapes, relations given in Refs. [30,31] can be used to express the ratio B_s between the surface areas of a deformed and a spherical liquid drop of the same volume (8) as

$$\begin{aligned} B_s = 1 &+ \frac{1}{2\pi}\,\alpha_{20}^2 - \frac{5}{210}\sqrt{\frac{5}{\pi}}\,\alpha_{20}^3 - \frac{33}{556\pi}\,\alpha_{20}^4 \\ &- \frac{3}{14\pi\sqrt{\pi}}\,\alpha_{20}^2\,\alpha_{40} + \frac{9}{4\pi}\,\alpha_{40}^2. \end{aligned} \tag{11}$$

A similar expression can be derived for the deformation dependence of the Coulomb energy [32].

In self-consistent models, however, the nuclear shape is naturally characterized by multipole moments of the local (mass) density, which are the expectation value of the operators $\hat{Q}_{\ell m} \equiv r^\ell\, Y_{\ell m}(\mathbf{r})$. Their values can be cast into the dimensionless deformations [22]

$$\beta_{\ell m} = \frac{4\pi}{3R_0^\ell A}\langle \hat{Q}_{\ell m}\rangle, \tag{12}$$

where $R_0 = 1.2\,A^{1/3}$ fm. These deformations are similar in size to the shape expansion parameters of Eq. (10), but not equivalent. Indeed, adapting the expressions of Refs. [30,31] to this expansion, for an axial liquid drop characterized by α_{20} and α_{40}, the corresponding quadrupole and hexadecapole moments are

$$\begin{aligned} \beta_{20} &= \alpha_{20} + \frac{2}{7}\sqrt{\frac{5}{\pi}}\,\alpha_{20}^2 + \frac{20}{77}\sqrt{\frac{5}{\pi}}\,\alpha_{40}^2 + \frac{12}{7\sqrt{\pi}}\,\alpha_{20}\,\alpha_{40} \\ &\quad - \frac{5}{28\pi}\,\alpha_{20}^3 - \frac{235}{924\pi}\sqrt{\frac{5}{\pi}}\,\alpha_{20}^4 + \frac{216\sqrt{5}}{77\pi}\,\alpha_{20}^2\,\alpha_{40}, \\ \beta_{40} &= \alpha_{40} + \frac{9}{7\sqrt{\pi}}\,\alpha_{20}^2 + \frac{300}{77\sqrt{5\pi}}\,\alpha_{20}\,\alpha_{40} \\ &\quad + \frac{275}{77\pi\sqrt{5}}\,\alpha_{20}^3 + \frac{33975}{4004\pi\sqrt{\pi}}\,\alpha_{20}^4, \end{aligned} \tag{13}$$

where we have limited ourselves to fourth order in deformation, assuming that α_{40} is on the order of α_{20}^2. Note that the expressions given in Ref. [22] use an inconsistent power counting, dropping terms in α_{20}^3 and α_{20}^4 while keeping terms in α_{40}^2. The necessary extension to include also octupole distortions is discussed for example in Refs. [33,34].

For a given self-consistent nuclear configuration characterized by deformations $\{\beta_{20}, \beta_{40}\}$, Eq. (13) can be numerically inverted to estimate the expansion parameters α_{20} and α_{40} of a liquid drop that has the same multipole moments. From these values, the corresponding LDM surface energy can then be estimated through Eq. (8).

This approximate mapping of deformations can be expected to be reliable only at small deformations for which powers of the $\alpha_{\ell 0}$ remain smaller than $\alpha_{\ell 0}$ itself and where the higher-order deformations that are neglected in Eq. (13) do not play a significant role yet.

For light nuclei, the LDM gives a spherical minimum and a broad single-humped fission barrier that becomes lower with increasing charge number Z. Neglecting the possible deformation dependence of the Coulomb exchange term, for a LDM model parametrized through Eq. (8) the fission barrier vanishes when $E_{\rm def} = (a_{\rm surf} + a_{\rm ssym} I^2) A^{2/3}(B_s - 1) + a_c Z^2 A^{-1/3}(B_c - 1)$ becomes negative for arbitrary shape distortions. Keeping only the leading term in the development of $B_s(\text{shape}) \approx 1 + \frac{1}{2\pi}\alpha_{20}^2 + \cdots$ from Eq. (11) and of $B_c(\text{shape}) \approx 1 - \frac{1}{4\pi}\alpha_{20}^2 + \cdots$ [32] at small distortions of a sphere, this can be expressed through the condition that the so-called *fissility parameter* x [30,35,36],

$$x = \frac{E_{\rm Coul}}{2\,E_{\rm surf}} = \frac{3\,e^2}{10\,r_0}\,\frac{Z^2}{(a_{\rm surf} + a_{\rm ssym}\, I^2)\,A}, \tag{14}$$

becomes larger than 1. As a consequence, very heavy nuclides with $x > 1$, which for typical values of the LDM coefficients correspond to $Z \gtrsim 104$, only exist because of quantal shell effects. The exact location of the $x = 1$ line depends of course on the values of the LDM parameters and can be very different for different Skyrme EDFs [13].

The concept of fissility has first been introduced for charged drops of macroscopic liquids, for which it can also be directly experimentally studied in great detail [37].

IV. RESULTS

A. Numerical choices

The calculations were all performed using the `MOCCa` code [38,39] that uses a coordinate-space representation. It is based

on the same principles as the published EV8 code [22,40]. The mesh parameter of the Lagrange-mesh representation [41,42] is set to $dx = 0.8$ fm for all nuclei, with a suitable box size adapted to each case. With the choices made, the numerical accuracy for the total energies that are presented here is better than 100 keV, independent of the deformation [43].

It is well known that the correct description of the fission path usually requires us to explore nonaxial and octupole deformations. The use of the MOCCa code permits us to do it in a general and consistent way.

Throughout this study, we use dimensionless mass multipole moments (12) to characterize deformation. Unless noted otherwise, nuclei are oriented in such a way that axially symmetric states are aligned with the z axis. When plotting deformation energy curves as a function of the quadrupole moment β_{20}, positive values of β_{20} indicate prolate shapes and negative values indicate oblate shapes. We also discuss deformation energy surfaces of triaxial systems in the β-γ plane defined through [22]

$$\beta = \sqrt{\beta_{20}^2 + 2\beta_{22}^2}, \tag{15}$$

$$\gamma = \text{atan2}(\sqrt{2}\,\beta_{22}, \beta_{20}). \tag{16}$$

To compare with experimental data for charge deformation obtained from in-band $E2$ transitions, we also need charge deformations $\beta_{\ell m,p}$, which are obtained from the multipole moments $\langle \hat{Q}_{\ell m,p} \rangle$ of protons as

$$\beta_{\ell m,p} = \frac{4\pi}{3R_0^\ell Z} \langle \hat{Q}_{\ell m,p} \rangle. \tag{17}$$

In a self-consistent mean-field model, values for $\beta_{\ell m,p}$ might differ on the percent level from the mass deformations $\beta_{\ell m}$ defined through Eq. (12).

B. Fission barriers

As fission barriers probe the deformation energy up to very large deformation [35,44,45], they are the natural starting point to explore correlations between observables and the surface energy coefficient. Here, we discuss three nuclei whose energy surfaces each have a different topography.

(i) The double-humped fission barrier of ^{240}Pu has been used as the reference case for many studies of different aspects of the fission process and its modeling in an EDF framework [1,8,10,12,18,46–53].

(ii) The slightly lighter nucleus ^{226}Ra is octupole-deformed in its ground state and many calculations agree on the prediction of a triple-humped fission barrier [52].

(iii) The observation that the very neutron-deficient nucleus ^{180}Hg fissions asymmetrically [54] is an illustration that the shell effects in highly deformed configurations along the fission path determine the most probable fission yields [54–58], not the shell effects in the fragments, which would favor a symmetric split into two ^{90}Zr.

This selection of systems has been motivated by the diversity of their energy landscape, by their spread location in the chart of nuclei covering a relatively wide range in mass and isospin, and by their fission path that can be comparatively easily followed in calculations with a single constraint. For many other systems, this is not the case, and multidimensional calculations have to be carried out in order to reliably find the saddle points [59].

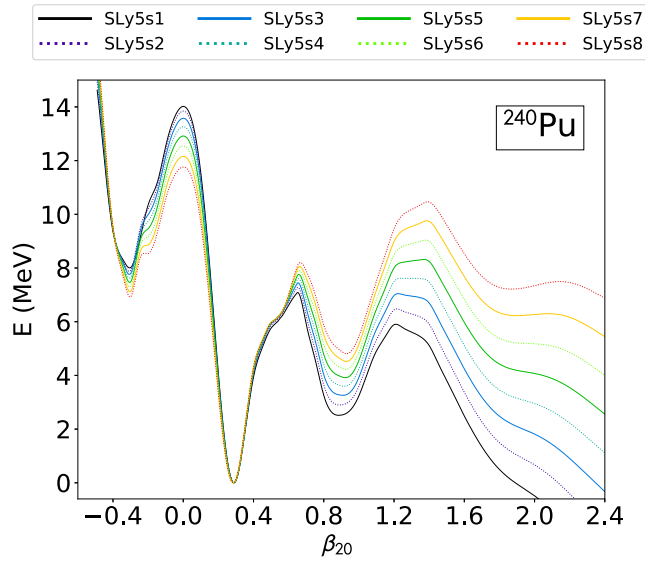

FIG. 2. Deformation energy curve of ^{240}Pu as a function of β_{20} for the parametrizations as indicated. The energies are normalized to the respective ground-state energy.

Calculations have been performed assuming time-reversal invariance and imposing two plane symmetries of the nuclear densities by choosing the single-particle states to be eigenstates of z-signature $\hat{R}_z$ and the y-time-simplex $\hat{S}_y^T$.

Only the lowest continuous static fission path as obtained from calculations allowing for both reflection-asymmetry and nonaxiality is presented. We first discuss the changes in the topography of the energy curves of these three nuclei when systematically varying the surface energy coefficient, and compare with experiment later on.

1. *Fission barrier of* ^{240}Pu

The fission barrier of ^{240}Pu is shown in Fig. 2. We have checked that the configurations along the fission path change continuously without sudden jumps. The fission path is practically the same for all SLy5sX parametrizations, with the deformation parameters $\beta_{\ell m}$ (12) taking near-identical values.

Up to the superdeformed minimum associated with the fission isomer, the lowest configurations are reflection symmetric. For larger deformations, octupole deformation sets in. Around the top of the inner and outer barriers at $\beta_{20} \simeq 0.5$ and $\beta_{20} \simeq 1.3$, respectively, the saddle points are lowered by nonaxial shapes, by about 1.5 MeV for the inner barrier and about 0.5 MeV for the outer barrier.[1] The corresponding γ angles (16) go up to about 12 degrees for the inner and 1.5

[1]When calculating the energy curves of ^{240}Pu as obtained with the SLy5sX reported in Ref. [8] we failed to find the nonaxial solution of the outer barrier. The energy curves shown there differ from Fig. 2 also by the use of HF+BCS instead of HFB.

degrees for the outer barrier, which corresponds to values of β_{22} of about 0.07 and 0.02, respectively.

With $\beta_{20,p}$ taking values between 0.293 for SLy5s1 and 0.287 for SLy5s8, the ground-state deformation agrees very well with the charge quadrupole deformation $\beta_{20,p} = 0.293 \pm 0.002$ that can be deduced with the usual expressions [12] from the experimental $B(E2; 0^+ \to 2^+)$ value [60]. Similarly, the calculated values for the charge hexadecapole deformation $\beta_{40,p}$ that fall between 0.164 for SLy5s1 and 0.155 for SLy5s8 also agree with the value $\beta_{40,p} = 0.166 \pm 0.040$ extracted from the measured $B(E4; 0^+ \to 4^+)$ that has been reported in Ref. [60]. Note that in the full β-γ plane, the oblate saddle at $\beta_{20} \simeq -0.3$ is connected without barrier to the prolate minimum through triaxial shapes.

As expected, going from SLy5s8 with its high value of $a_{\rm sym}$ to SLy5s1 with its low one, the deformation energy relative to the ground state is significantly reduced for states that have a larger deformation than the ground state. This reduction is quite uniform, such that at a given deformation the curves are almost equally spaced, and their spread almost uniformly increases with deformation. That the order of the curves is inverted around the spherical point and for oblate shapes is a consequence of normalizing all energies relative to the deformed ground state. Qualitatively, the same spread of the energy curves that is visible when going from the prolate ground state to the superdeformed state also happens when going from the spherical state to the deformed ground state, although on a smaller energy scale. But since energies are normalized to the more deformed one among the two states, the order of the curves becomes inverted when going from the ground state to smaller deformations instead of larger ones. The same artifact from normalization also appears on several other plots discussed in what follows.

The increasing change of deformation energy as a function of deformation that accompanies a change in $a_{\rm surf}$ can make shallow minima appear or disappear, as can be seen from the third hyperdeformed minimum at $\beta_{20} \simeq 1.8$ that is predicted by SLy5s8. Going to parametrizations with lower $a_{\rm surf}$ it gradually vanishes as the downfalling slope of the energy becomes increasingly steep.

Quantitatively, reducing $a_{\rm surf}$ by 7.2% when going from SLy5s8 to SLy5s1 reduces the outer barrier by about 5 MeV, which is about 40% in this case. The relative height of the inner and outer barriers is also reversed: for SLy5s8 it is the outer barrier that is the highest one, whereas for SLy5s1 it is the inner barrier. Both differences would have an enormous impact on fission dynamics calculated with one or the other of these parametrizations.

2. *Fission barrier of* ^{226}Ra

The energy curves for ^{226}Ra are shown in Fig. 3. Again, all parametrizations give the same fission path. This nucleus is located in a small region of the nuclear chart where stable octupole deformations are present in the ground state, leading to an energy gain of a couple of 100 keV compared to the reflection-symmetric saddle. The values are slightly increasing with decreasing $a_{\rm surf}$, from about 250 keV for SLy5s8 to about 700 keV for SLy5s1. The actual octupole deformation of the ground state also sensitively depends on the parametrization, and increases with decreasing $a_{\rm surf}$ from $\beta_{30} = 0.06$ for SLy5s8 to $\beta_{30} = 0.12$ for SLy5s1. A similar behavior is found for the majority of nuclides with octupole-deformed ground state; see the discussion in Sec. IV H 1. Around $\beta_{20} \simeq 0.5$, the first barrier proceeds through a region of reflection-symmetric, but triaxial, configurations. Around the superdeformed minimum at $\beta_{20} \simeq 0.7$, the lowest states become axial and reflection symmetric. From the second barrier onwards, the lowest states take reflection-asymmetric shapes, including the ones in the third minimum around $\beta_{20} \simeq 1.5$. A detailed comparison of the lowest energy curve obtained with SLy5s1 with the ones obtained when imposing reflection symmetry and/or axiality can be found in Ref. [61]. We have not found any reduction of the outer barriers when allowing for nonaxial shapes.

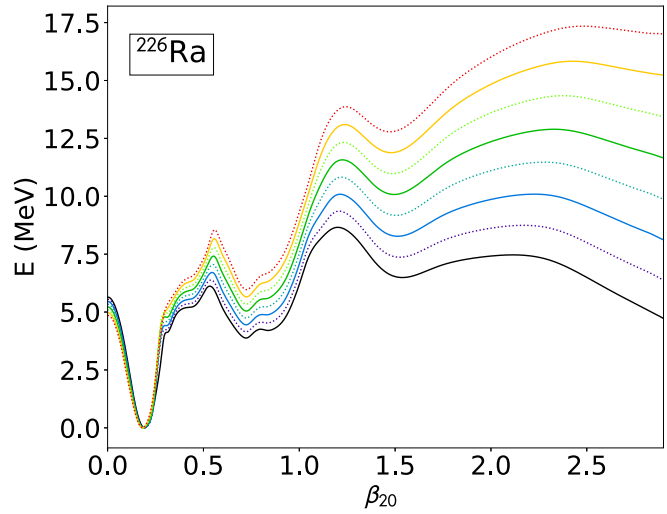

FIG. 3. Same as Fig. 2, but for ^{226}Ra.

The calculated ground-state proton quadrupole moment takes values between $\beta_{20,p} = 0.161$ (SLy5s8) and 0.169 (SLy5s1), which somewhat underestimates the empirical value $\beta_{20,p} = 0.202(3)$ determined from the experimental $B(E2; 0^+ \to 2^+)$ value [34] for all parametrizations.

The evolution of differences between parametrizations with deformation are qualitatively the same as what was found for ^{240}Pu. As the outermost barrier is at larger deformation, its overall reduction when going from SLy5s8 to SLy5s1 is even more dramatic. Again the difference of barrier heights changes sign, here for the second and third barriers. The broad third barrier found with SLy5s8 almost becomes a shoulder with SLy5s1, thereby making the third minimum very shallow.

3. *Fission barrier of* ^{180}Hg

Figure 4 displays the fission barrier of ^{180}Hg. Again, all parametrizations lead to the same fission path. The energy landscape of this nucleus differs from the other two discussed above in several respects: First, it exhibits shape coexistence at small deformation. Second, there is only one broad barrier, whose saddle point is at much larger deformation. Third, the

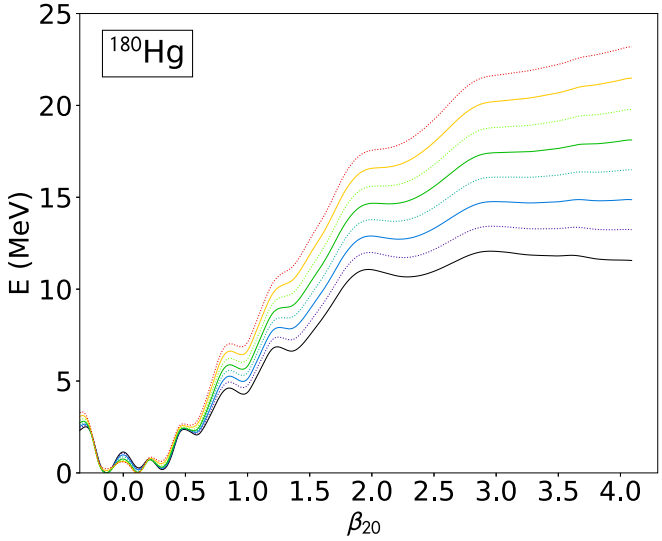

FIG. 4. Same as Fig. 2, but for ^{180}Hg.

scission point, where the fissioning nucleus breaks apart, is very close to the top of the barrier. The curves in Fig. 4 end where the calculations jump to a different solution, with two nonidentical fragments, that is about 30 MeV below. There are also several superdeformed and hyperdeformed local minima visible between the normal-deformed minima and the barrier, a feature already found in earlier calculations of this nucleus. We have not checked if the barriers separating these structures become lower or even disappear when allowing for nonaxial shapes. The broad outer barrier follows a reflection-asymmetric path beginning at around $\beta_{20} \simeq 1.1$, such that the shallow minimum at slightly larger deformation exhibited by SLy5s1 corresponds to octupole deformed shapes. We have not found nonaxial solutions that lower the barrier at these large deformations.

The evolution of differences between parametrizations with deformation is again qualitatively the same as what was found above for ^{240}Pu and ^{226}Ra. As the outermost barrier is at larger deformation, the overall variation of barrier height is even more dramatic. Again, the position of the saddle point changes: it moves from $\beta_{20} \simeq 4.0$ to $\beta_{20} \simeq 3.0$ when going from SLy5s8 to SLy5s1.

We mention in passing that the deformation of the ground state changes from weakly oblate for parametrizations with low $a_{\rm surf}$ up to SLy5s4 to weakly prolate for parametrizations with higher $a_{\rm surf}$. The same also happens for some of the adjacent Hg isotopes, which has an impact on the evolution of charge radii and their odd-even staggering. As has been discussed elsewhere [62], the parametrizations with low $a_{\rm surf}$ provide a much better description of these data than the ones with high $a_{\rm surf}$.

4. Correlation between characteristic energies and a_{surf}

The energy curves presented above indicate that for the SLy5sX parametrizations the differences between deformation energies scale with the surface energy coefficient $a_{\rm surf}$ and the deformation. This is confirmed when plotting some

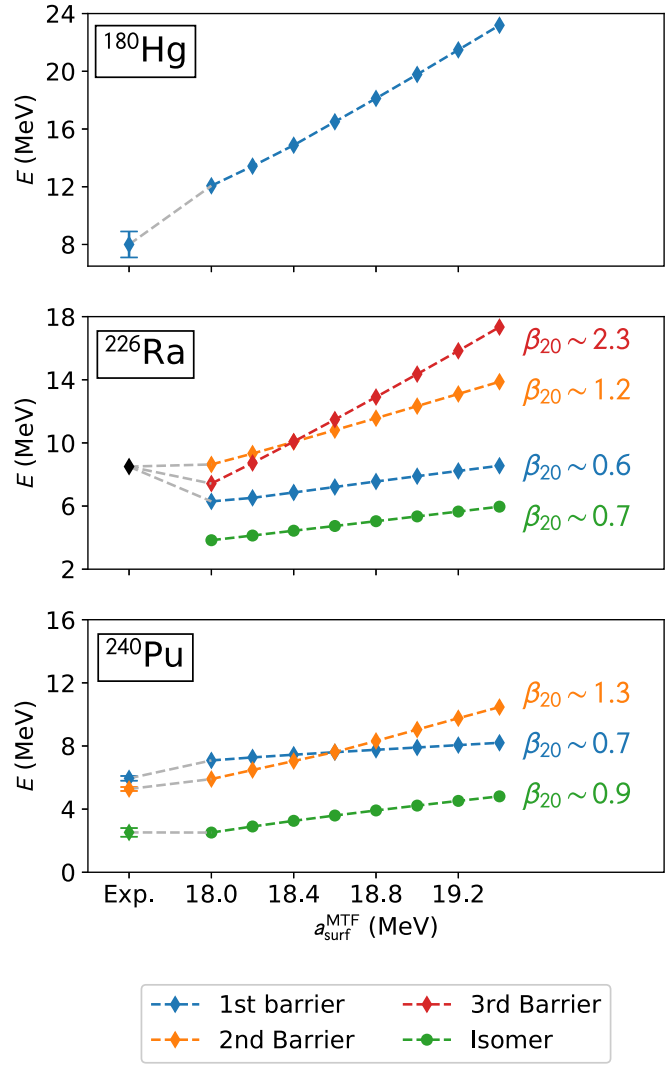

FIG. 5. Height of the first ($E_{\rm 1st}$), second ($E_{\rm 2nd}$), and third ($E_{\rm 3rd}$) barrier as well as the excitation energy of the fission isomer ($E_{\rm iso}$) of the nuclei as indicated vs the surface energy coefficient $a_{\rm surf}$ calculated in the MTF model as used as a constraint in the fit of the SLy5sX parametrizations.

characteristic energies such as the heights of various barriers and excitation energies of the superdeformed states for these nuclei directly as a function of $a_{\rm surf}$; see Fig. 5.

The deformation dependence (8) of the LDM (6) predicts that for a given nucleus at a given shape with fixed deformation parameters the total energy is a linear function of $a_{\rm surf}$. And indeed, all curves are almost linear, with the most pronounced deviation for the barrier height of ^{180}Hg, although even there the slight bend of this curve is just barely visible. The reason for the latter is that the saddle point gradually changes its deformation from $\beta_{20} \simeq 4$ to $\beta_{20} \simeq 3$ when lowering $a_{\rm surf}$; cf. Fig. 4.

This plot confirms the validity of the idea of Ref. [8] that the adjustment of interactions to characteristic energies of fission barriers can be replaced by the adjustment of a suitably chosen value of $a_{\rm surf}$.

To the left in Fig. 5, we provide experimental data, where available, for comparison. We recall, however, that the empirical determination of fission barrier heights and excitation energies of fission isomers is not trivial and, in general, requires the application of some model. Calculated fission barriers are usually those of the ground state, whereas in experiment they are most often probed through the decay of excited states. For ^{240}Pu, the error bars cover the range of the values reported in Refs. [44,53,63–65]. The barrier height of 8.5 MeV for ^{226}Ra is the recommended value from the RIPL-3 database [63]. The situation is more complicated for ^{180}Hg, for which data come from the observation of β-delayed fission of ^{180}Tl, which passes through excited states of negative parity and finite angular momentum at an excitation energy that is necessarily smaller than the Q value for electron capture of ^{180}Tl, $Q_{\rm EC}(^{180}{\rm Tl}) = 10.44$ MeV. The model-dependent analysis of the measured probability of β-delayed fission in that nucleus [55] suggests that the fission barrier has a height of about 8.0(9) MeV, which is the value used in Fig. 5.

None of the parametrizations reproduces all data simultaneously, but it is obvious that those with the smallest values of $a_{\rm surf}$ in the set are clearly favored. Compared to the other parametrizations, SLy5s1 gives a fair description of the available data for ^{240}Pu and ^{226}Ra, but still significantly overestimates the barrier for ^{180}Hg. The latter, however, is the most uncertain value in the data set. Macroscopic-microscopic models that describe well the fission barriers of actinide nuclei also give a barrier height of ^{180}Hg that is too high by about 2 MeV [55]. We recall that many widely used parametrizations of the Skyrme EDF such as SLy4 have a surface energy coefficient that, when calculated in the MTF model, take values about 19.0 ± 0.3 MeV [8] and then overestimate fission barriers, while the often-used standard for fission studies, SkM*, has an $a_{\rm surf}$ of a similar size as SLy5s1.

There are many possible reasons for the scatter of the deviations from data. First, shell effects might be incorrect, either in the ground state or for the saddle point or both. Indeed, the complicated structure of the deformation energy curves of Figs. 2–4 with its multiple maxima and minima at various deformations is determined by shell effects. Without them, these three nuclei would have a spherical ground state and one broad fission barrier without any substructure. Second, the isospin dependence of the surface energy of the SLy5sX might be incorrect. This, however, cannot be corrected for by simply increasing the absolute value of the (negative) surface symmetry energy coefficient $a_{\rm ssym}$ in Eq. (6). With $I^2 = (20/180)^2 \approx 0.012$, the asymmetry of ^{180}Hg is much smaller than the one of ^{240}Pu, $I^2 = (52/240)^2 \approx 0.047$ such that the reduction of the barrier of the latter would be greater. Instead, one has to change both $a_{\rm surf}$ and $a_{\rm ssym}$ in order to reproduce both barriers simultaneously. Assuming that the entire change of the outer fission barrier heights of ^{180}Hg and ^{240}Pu between SLy5s8 and SLy5s1 is due to the change in their effective surface energy coefficient (7), one can estimate values that would describe both barriers through linear extrapolation. Reproducing the outer barrier height of 5.3 MeV of ^{240}Pu with a parametrization adjusted along the lines of the SLy5sX calls for an effective surface energy coefficient

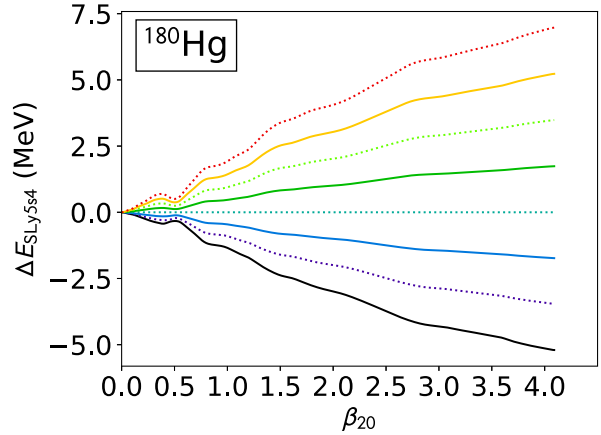

FIG. 6. Difference $E^{\rm SLy5sX}({\rm shape}) - E^{\rm SLy5s4}({\rm shape})$ between the deformation energy of ^{180}Hg as obtained with the SLy5sX parametrizations and shown in Fig. 4 and the deformation energy obtained with SLy5s4. The same color code as in Fig. 2 is used.

$a^{\rm HF}_{\rm surf,eff}(146, 94) \simeq 15.14$ MeV, whereas reproducing the recommended value of 8.0 MeV for the barrier height of ^{180}Hg from Ref. [55] demands for $a^{\rm HF}_{\rm surf,eff}(100, 80) \simeq 16.49$ MeV. To obtain such values requires us to set $a^{\rm HF}_{\rm surf} \approx 16.97$ MeV and $a^{\rm HF}_{\rm ssym} \approx -39$ MeV. Using the upper limit of 8.9 MeV for the estimated barrier height of ^{180}Hg instead yields $a^{\rm HF}_{\rm surf} \approx 17.11$ MeV and $a^{\rm HF}_{\rm ssym} \approx -42$ MeV instead. With that, the ratio of both would be reduced from $a^{\rm HF}_{\rm ssym}/a^{\rm HF}_{\rm surf} \approx -2.7$ for all SLy5sX to -2.3, and in absolute value become closer to the ratio of the volume coefficients, which takes values of about $a_{\rm vol}/a_{\rm sym} \approx 2$ for all SLy5sX. This analysis, however, assumes that shell effects are correctly described in both nuclei, which is not necessarily the case. While pushing the values for $a^{\rm HF}_{\rm surf}$ and $a^{\rm HF}_{\rm ssym}$ slightly outside the range of combinations found for the majority of parametrizations of Skyrme EDF, the changes suggested by the above analysis remain comparatively small, such that there is no *a priori* reason to rule them out. In fact, the modified values estimated from the barrier heights of ^{240}Pu and ^{180}Hg become very close to those of the modern Lublin-Strasbourg drop (LSD) parametrization of the LDM [66], $a^{\rm LSD}_{\rm surf} = 16.9707$ MeV and $a^{\rm LSD}_{\rm ssym} = -38.9274$ MeV, which has been adjusted to masses and fission barrier heights. Because of the model dependence of the actual values of the surface energy coefficients extracted from EDFs [8,29], however, it cannot be ruled out that this agreement is fortuitous.

We recall that the simple near-linear dependence of $E_{\rm def}({\rm shape})$ as a function of $a_{\rm surf}$ as exhibited by Fig. 5 can only be found when using a series of parametrizations that have been adjusted within the same dedicated protocol. Otherwise there is a large scatter around the global linear trends as exemplified in Ref. [8].

There is the question of how much, and for which configurations, shell effects do actually differ when going from one parametrization to another. Figure 6 shows the difference in deformation energy between SLy5s4 and the other SLy5sX parametrizations for prolate configurations up to the scission

point. The differences are clearly not simple straight lines as would be the case if the SLy5sX parametrizations only differed in their surface energy coefficient. Instead, there are oscillations around the linear trend that occur at the same deformation for all parametrizations, and whose amplitude increases when going to smaller deformation. The amplitude of these oscillations also increases with the difference in $a_{\rm surf}$ of the parametrizations. For this reason we choose to plot the difference to an intermediate parametrization, which allows for a better resolution of the deviations than plotting the difference to either SLy5s1 or SLy5s8. The deformations where the most pronounced of these oscillations are situated correspond to the barrier below the SD minimum ($\beta_{20} \approx 0.4$), the SD minimum ($\beta_{20} \approx 0.6$), and the barriers between the highly deformed minima ($\beta_{20} \approx 0.4, 0.9, 1.2, ...$).

Limiting the discussion to small deformations below $\beta_{20} = 0.7$ where the expansion (10) of the nuclear surface can be expected to approximately match the actual shape of the self-consistent solutions, Fig. 7 provides estimates of the contribution from the LDM surface energy and shell effects to the deformation energy of ^{180}Hg.

The upper panel shows again the deformation energy as obtained from self-consistent calculations, but unlike Fig. 4 the energies are now normalized to the spherical shape. To estimate the LDM surface energy, the deformations α_{20} and α_{40} entering the expression for the deformed liquid drop (10) are determined from the deformations β_{20} and β_{40} of the self-consistent states by inversion of relations (13). From these, the deformation-dependent LDM surface energy $E^{\rm surf}_{\rm LDM}$(shape) is calculated by inserting (11) into (8). This is done separately for the results obtained with each SLy5sX parametrization, using the respective effective surface energy coefficient (7) constructed from the HF values of $a_{\rm surf}$ and $a_{\rm ssym}$ taken from Table II. As we are only interested in relative changes, the LDM surface energy obtained from SLy5s1 is subtracted from all curves. The actual LDM deformation energy changes by about 25 MeV over the range of the plot, most of which is compensated by an almost as large change in Coulomb energy. The shapes found along the path of lowest energy are almost independent of the parametrization, such that the difference between the LDM surface energies $E^{\rm surf}_{\rm LDM}$(shape) of the various SLy5sX is simply monotonically growing with β_{20} as it is entirely determined by the differences in $a_{\rm surf,eff}$. However, as the surface area of a liquid drop, Eq. (8), is a complicated function of β_{20} with the leading term being quadratic, the curves for the $E^{\rm surf}_{\rm LDM}$(shape) are not straight lines themselves. It is only at a given deformation that the distance between two curves can be expected to be proportional to the difference in $a_{\rm surf}$ between the parametrizations they were constructed with.

Having deduced the LDM deformation energy, we can also estimate "microscopic" shell energies that are at the origin of the minima and maxima of the self-consistent energy curve. Such quantity can be constructed by subtracting the deformation dependent parts of the LDM surface energy $E^{\rm surf}_{\rm LDM}$(shape) and the self-consistent Coulomb energy, calculated through Eq. (9), from the total binding energy from the EDF. The resulting energy curves, normalized to the spherical point, are shown in the lower panel. For obvious reasons their local minima coincide with the local minima of the energy curves from self-consistent calculations in the upper panel, and the maxima with the barriers in between.

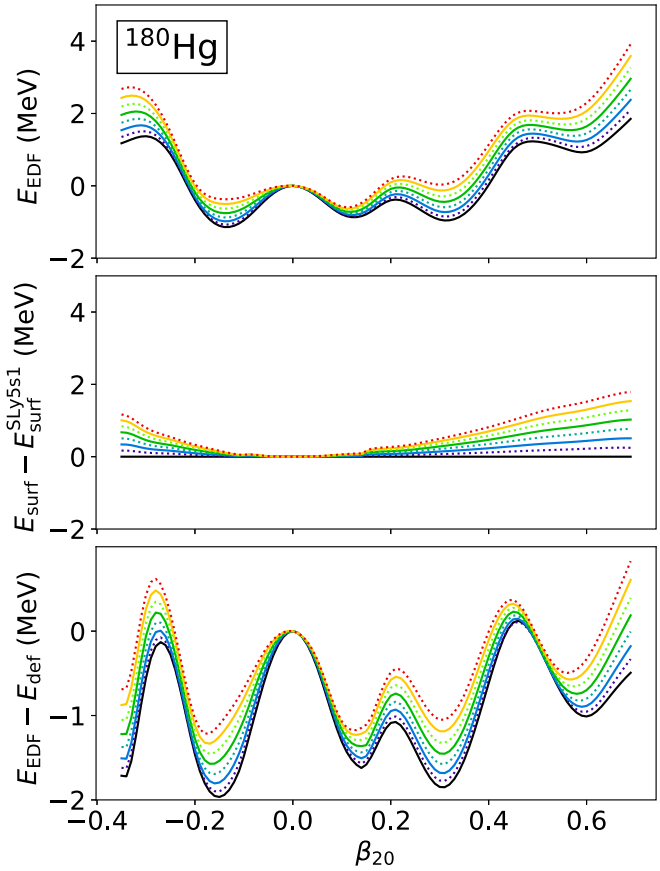

FIG. 7. Deformation energy of ^{180}Hg as obtained from self-consistent calculations (top), difference between the surface energies $E^{\rm surf}_{\rm LDM}$(shape), defined through (8), of a deformed liquid drop (10) that yields the same multipole deformations β_{20} and β_{40} as the self-consistent calculation (middle), and the evolution of shell effects estimated by subtracting the LDM deformation energy (9) from the energy of the self-consistent calculations. All curves are drawn as a function of the axial quadrupole deformation β_{20} and normalized to the energy at spherical shape, and the same color code as in Fig. 2 is used to distinguish the SLy5sX parametrizations. Note that the same energy interval is used for the upper two panels.

Comparing the results obtained with different SLy5sX parametrizations, the amplitude of the variations of shell effects along the path of lowest energy differs on the scale of about 1 MeV. It is smallest for SLy5s8 and largest for SLy5s1. This variation is correlated to the size of the spin-orbit coupling constant $C_0^{\rho\nabla\cdot J}$, see Table II, which has a significant impact on the position of some specific single-particle states near the Fermi surface; see the discussion of Fig. 14 in what follows.

It has to be stressed that this "microscopic" energy is not completely equivalent to a shell correction as defined through the Strutinski theorem [2–5]. Besides imperfections of the mapping on the LDM surface energy, this energy also contains the neglected higher-order contribution to the LDM energy,

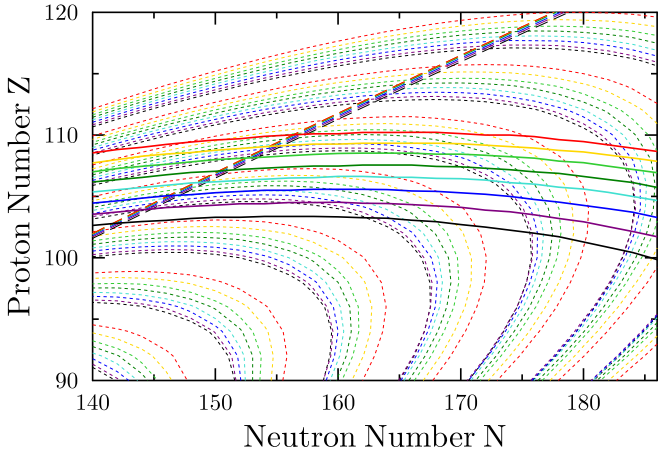

FIG. 8. Gross properties of superheavy nuclei as obtained from the LDM parameters of the SLy5sX parametrizations. Using the same color code for the parametrizations as in Fig. 2, the light dotted lines show the contours of E/A of spherical nuclei, varying between -7.6 MeV in the lower left corner and -7.0 MeV in the upper left corner in steps of 100 keV. The heavy dashed lines show the proton drip line defined through $S_{2p}(N, Z) = 0$, whereas the heavy solid lines indicate the line where fissility takes the value $x = 1$.

the deformation dependence of the pairing energy, as well as the deformation dependence of the tensor terms E_{JJ} in Eq. (2), which depends on the filling of shells. In addition, only the variation of this microscopic energy with deformation can be determined from our mapping, not its absolute size.

Still, the results indicate that, in spite of their identical fit protocol, rearrangement effects during the parameter fit lead to changes between the SLy5sX parametrizations such that the shell effects of the ground state of ^{180}Hg vary by about 1 MeV. For other nuclei the changes might even be larger, as the amplitude of the variation of shell effects itself is larger. Unfortunately, the analysis of shell effects outlined above becomes much more involved when nonaxial or reflection-asymmetric deformations come into play, as is the case for the static fission paths of ^{226}Ra and ^{240}Pu.

C. Superheavy nuclei

In the discussion of ^{180}Hg, ^{226}Ra, and ^{240}Pu, we have seen that the outer saddle point tends to move to smaller deformation. As outlined in Sec. III, the LDM fission barrier becomes smaller with increasing charge number Z until it vanishes for nuclei for which the fissility x, as defined in Eq. (14), becomes larger than 1. In fact, fissility is an often used criterion to define the so-called superheavy elements as those that have a vanishing liquid-drop fission barrier and only exist because the quickly fluctuating shell effects still generate a fission barrier [67].

Figure 8 shows the line of fissility $x = 1$ in the region of known transactinide nuclei, calculated by inserting the INM parameters as listed in Table I and the HF values for the surface and surface symmetry energy coefficients from Table II in Eq. (14). The figure also shows the lines of equal $E_{\rm LDM}/A$ and the position of the two-proton dripline, where $S_{2p}(N, Z) \equiv E_{\rm LDM}(N, Z-2) - E_{\rm LDM}(N, Z)$ becomes zero.

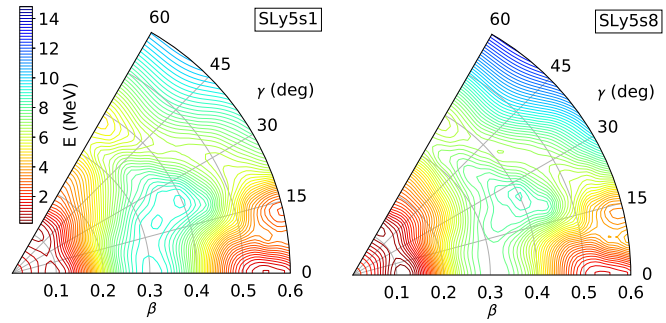

FIG. 9. Deformation energy surface of ^{294}Og using the SLy5s1 (left) and SLy5s8 (right) parametrizations from calculations assuming reflection-symmetric triaxal shapes. The energies are normalized to the respective ground-state minimum that has been determined by interpolation of the calculated points on the surface.

The relative displacement of lines of equal E/A indicates clearly that for the SLy5sX parametrizations the (negative) LDM binding energy $E_{\rm LDM}(N, Z)$ of a given nucleus takes larger absolute values when increasing $a_{\rm surf}$. This clearly points to large rearrangement effects during the parameter fit, as increasing $a_{\rm surf}$ in the LDM energy (6) while keeping all other parameters constant would decrease the absolute value of the binding energy. By contrast, the position of the two-proton drip line calculated from the LDM binding energies is practically the same. This is the consequence of another rearrangement effect in the coupling constants during the fit that is elaborated in more detail in Sec. IV F below.

We note in passing that, because of its A and I^2 dependence, the value of the fissility is not the same for all isotopes of an element with given Z, which introduces some ambiguity into the definition of superheavy elements as those for which $x > 1$.

As an example of the deformation energy of a superheavy nucleus, Fig. 9 displays the energy surfaces in the β-γ plane of ^{294}Og ($Z = 118$, $N = 176$), that is the heaviest even-even nucleus identified in experiment so far [68]. Results are only shown for SLy5s1 and SLy5s8, the parametrizations at the extremes of the interval of $a_{\rm surf}$. Unlike the cases of lighter nuclei discussed above, the fission path is not exactly the same, although its gross features remain similar for both parametrizations.

This nucleus, which is in a region of transitional nuclei close to the next spherical shell closures, has a quite complicated deformation energy surface, such that a path of lowest energy cannot be easily calculated and represented as a function of a single deformation parameter. Indeed, at deformations below $\beta_2 \lesssim 0.15$, the energy surface is quite flat, with the absolute minimum being on the prolate side for SLy5s8, whereas it is oblate for SLy5s1. The static fission path proceeds through axial oblate shapes before turning towards triaxial shapes. It bypasses an axial superdeformed prolate minimum at $\beta_{20} \approx 0.55$ and proceeds through a very shallow excited triaxial minimum at $\beta_2 \approx 0.6$, $\gamma \approx 15^\circ$ instead. Beyond the border of the plot, the energy of that valley continues to fall off. The outer barrier is further lowered when also allowing for nonaxial reflection-asymmetric shapes, but we

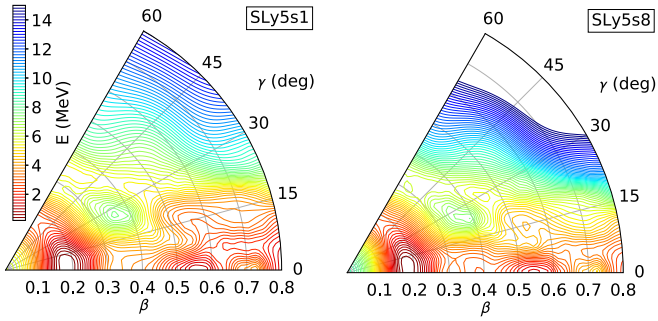

FIG. 10. Same as Fig. 9, but for ^{282}Cn.

have not systematically explored this degree of freedom. In any event, the inner barrier is higher than the outer one.

The difference in barrier height between SLy5s1 and SLy5s8 on this path of lowest energy remains very small; for the former it is about 6.1 MeV with the saddle reached for oblate shapes, while for the latter it is about 6.5 MeV reached at triaxial shapes. This is much smaller than what has been found for the differences between inner barriers of ^{226}Ra or ^{240}Pu. The reasons for this different behavior are that on the one hand the underlying LDM energy surface is very flat, and on the other hand the variation of shell effects is clearly not the same as evidenced by the many small differences in the topography of the energy surfaces. This is particularly obvious when looking at the excited fission path that passes through near-axial shapes on the prolate side of the β-γ plane: with slightly more than 8.4 MeV, it is higher for SLy5s1 than for SLy5s8, which gives only about 7.6 MeV. It is only at larger deformation beyond $\beta_2 \gtrsim 0.5$ that the energy surface obtained with SLy5s8 is visibly stiffer than the one from SLy5s1 as one would naively expect. The axial superdeformed minimum has about 0.25 MeV excitation energy for SLy5s1, whereas it is at 1.25 MeV for SLy5s8.

The few observed α-decay chains of ^{294}Og end with ^{282}Cn ($Z = 112$, $N = 170$) [68], a nucleus whose decay is dominated by spontaneous fission. The energy surfaces obtained for this nucleus are shown in Fig. 10. Passing through near-axial prolate shapes, the calculated static fission path of ^{282}Cn is rather similar to the one of heavy actinides. Both parametrizations agree on a prolate ground state, and also give a shallow excited axial superdeformed minimum at $\beta_{20} \simeq 0.55$, whose excitation energy is less than 1 MeV. With about 3.6 MeV, the inner barrier is higher for SLy5s1 than for SLy5s8, for which it takes a value of about 3.0 MeV, similar to what has been found for the excited near-axial path for ^{294}Og. It is again only for the outer barrier that SLy5s8 gives a larger height than SLy5s1, as one would expect from their values for $a_{\rm surf}$. For both parametrizations, the outer barrier passes again through triaxial shapes, and continues to fall off outside the border of the plots. With 3.2 MeV, it is minimally higher than the inner one for SLy5s8, whereas for SLy5s1 it is the other way around. Reflection-asymmetric shapes, not considered when preparing Fig. 10, lower again the energy surface for $\beta_2 \gtrsim 0.55$, such that it is the inner barrier which determines this nucleus' lifetime.

There also is a shallow excited valley connecting an excited triaxial minimum with oblate shapes through triaxial ones with large γ values, similar to the static fission path found for ^{294}Og in Fig. 9. On this path, with 6.2 MeV, the saddle from SLy5s8 is higher than the one at 5.6 MeV predicted by SLy5s1, similar to what has been found for ^{294}Og.

In any event, the fission barrier of ^{282}Cn is correctly predicted to be much lower than the one of ^{294}Og. However, these two examples illustrate that for superheavy nuclei at the limits of the presently known chart of nuclei there is not necessarily a direct correlation between fission barrier heights and the value of $a_{\rm surf}$. The structure of these nuclei with fissility larger than one is dominated by shell effects that, in spite of the common fit protocol, turn out to be slightly different for the SLy5sX parametrizations.

D. Superdeformed minima

Throughout the chart of nuclei, there are regions where one can find excited rotational bands with very large moments of inertia that extend to high spins well beyond $I \gtrsim 40$. These bands can be associated to shapes that have much larger deformations than what is found for ground states, with β_{20} taking values between 0.6 and 0.8. In heavy nuclei, such deformation brings single-particle levels originating from two major spherical shells above or below close to the Fermi energy. Because of the resulting significant difference in occupied orbits, electromagnetic decay out of these bands to normal-deformed (ND) states is in general hindered. Thanks to that, the bands can be followed over many transitions down to an end point where the decay out of the band takes place abruptly, with a very complicated highly fragmented multistep pattern of transitions. In many cases, the decay-out cannot be resolved in experiment [69]. This phenomenon has been dubbed superdeformation (SD) in the literature.

The SD bands found for nuclei in the neutron-deficient $A \simeq 190$ region are of special interest for our analysis, because for some of them the decay-out to ND yrast states occurs at low spins of about 10 $\hbar$, and with only a few intermediate steps that can be resolved in experiment. From the known excitation energies of states in the SD band, the excitation energy of the (unobserved) SD 0^+ band head can be estimated with a good accuracy [70–75].

One of these nuclides is ^{194}Hg. Figure 11 shows the variation of the total energy of this nucleus as a function of the axial quadrupole deformation. Besides normal-deformed prolate and oblate minima there is a superdeformed one at $\beta_{20} \simeq 0.65$. As for the other nuclei discussed so far, the overall topography of the energy surface is the same for all eight parametrizations, and differences between them grow larger as the deformation increases. The most pronounced minima are obtained with SLy5s1. With increasing $a_{\rm surf}$, the energy surface becomes overall stiffer, part of which is, however, because of a significant difference in shell effects between the parametrizations, similar to what has been found for ^{180}Hg. This becomes clearly visible when plotting the difference between the deformation energy obtained from different parametrizations; see Fig. 12. The curves do indeed not rise monotonically as they would if the surface tension were the only source of differences between the deformation energies.

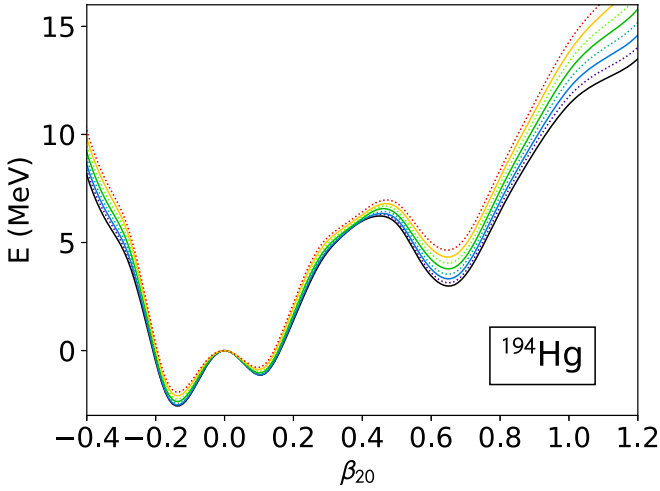

FIG. 11. Energy of ^{194}Hg as a function of axial quadrupole deformation parameter β_{20} for the SLy5sX parametrizations using the same color code as in Fig. 2. The energy is normalized to the spherical configuration.

Other neutron-deficient Hg isotopes in the $A \approx 190$ region exhibit energy curves with very similar structure, although the relative energy between the various minima and the height of the barriers separating them changes when going down in neutron number from $N = 120$ to $N = 106$; see Fig. 13. From the rapid variation of the excitation energy of the SD minimum and the barrier that separates it from ND states it is clear that there is a strong variation of neutron shell effects at large deformation with neutron number. The deformation of the SD minimum varies only very little, however, which indicates that it is mainly caused by a proton shell effect.

This is confirmed by the Nilsson diagrams of these nuclei. Figure 14 shows examples for ^{188}Hg, obtained with SLy5s1 and SLy5s8. There is a deformed $Z = 80$ gap at the deformation $\beta_{20} \simeq 0.65$ of the SD minimum. There also is a large deformed gap for neutrons at $N = 110$, but at slightly larger

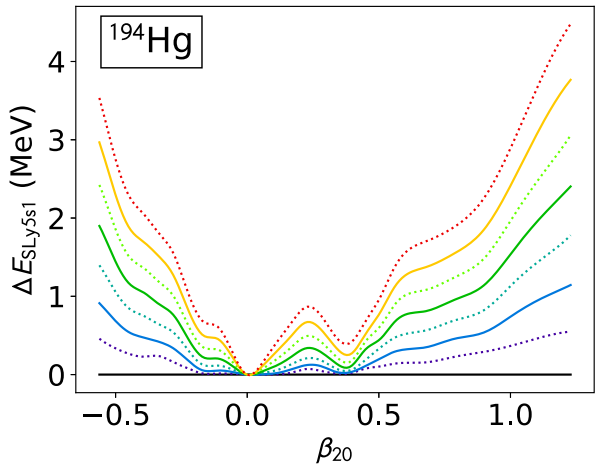

FIG. 12. Difference between the deformation energy of ^{194}Hg obtained with the SLy5sX parametrizations relative to the one obtained with SLy5s1. The same color code as in Fig. 2 is used.

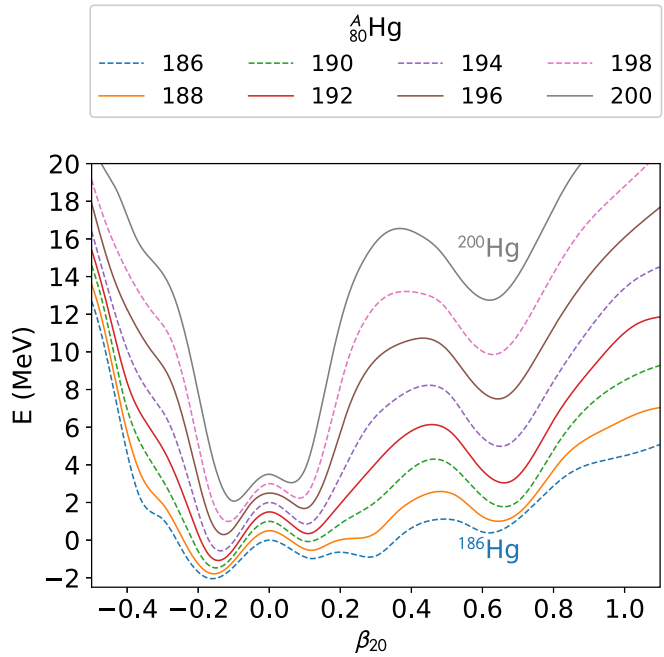

FIG. 13. Deformation energy of even-even Hg isotopes as a function of axial quadrupole moment β_{20} for the SLy5s1 parametrization. The energy curves are drawn with an offset of 0.5 MeV for the spherical state between two consecutive nuclei.

deformation $\beta_{20} \simeq 0.75$, which is not sufficient to generate an additional minimum. Instead, its main effect seems to be to soften or stiffen the energy curve at deformations larger than the one of the SD minimum. We recall that the shell effects on energy curves are generated by large deviations of the level density around the Fermi energy from the average one, and not by the actual size of the gaps between the levels. As the bunching of neutron levels above and below the $N = 110$ gap is much larger than what is found for proton levels around the $Z = 80$ gap, the net neutron shell effect on the energy curves is much weaker than the one of the protons, in spite of the size of the actual gap being larger.

At the deformation of the SD minimum, there are smaller neutron gaps for $N = 112$ and $N = 114$ that, however, are not of the same size for SLy5s1 and SLy5s8. This can be related to small differences between the relative position of spherical shells that can be attributed to the difference of spin-orbit coupling constants $C_t^{\rho\nabla\cdot J}$; cf. Table II. Spin-orbit splittings tend to be slightly larger for SLy5s1 than for SLy5s8, which then has a visible influence on the deformation dependence of shell effects that can be seen in Fig. 12. Its most obvious effect at spherical shape concerns the position of the high-j intruder level near the Fermi surface relative to the low-j levels around it. For SLy5s8 with its comparatively small $C_t^{\rho\nabla\cdot J}$ the neutron $i_{13/2^+}$ intruder level is between the $p_{1/2^-}$ and the quasidegenerate $f_{5/2^-}$ and $p_{3/2^-}$ levels, whereas for SLy5s1, with its 10% larger values of $C_t^{\rho\nabla\cdot J}$, the $i_{13/2^+}$ is pushed below the latter two levels. Similarly, for protons the $h_{11/2^-}$ intruder level is quasidegenerate with the $s_{1/2^+}$ level, whereas for SLy5s1 it is almost 1 MeV lower. These changes have a significant impact on the shell effects at small

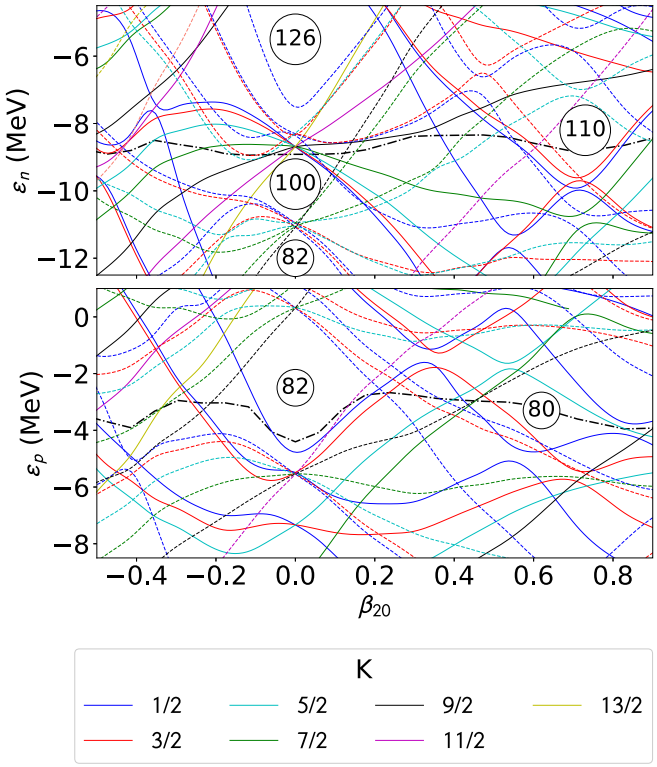

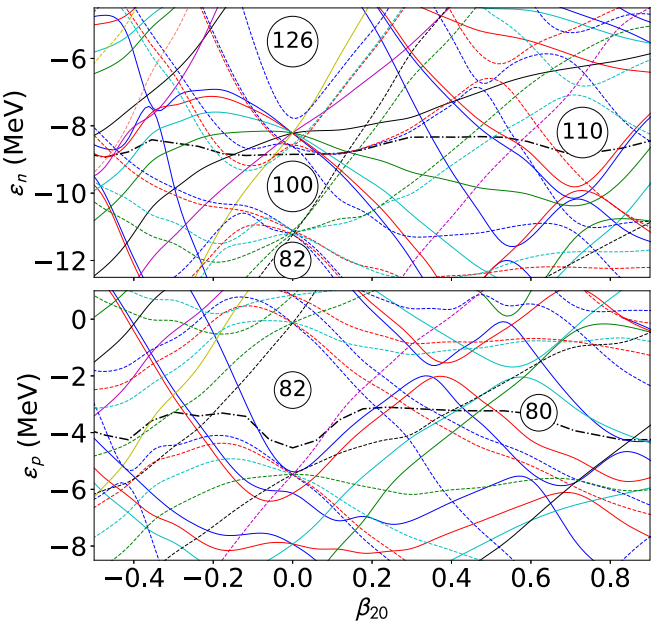

FIG. 14. Nilsson diagrams of eigenvalues of the single-particle Hamiltonian of neutrons (ϵ_n) and protons (ϵ_p) for axially symmetric states of ^{188}Hg obtained with the SLy5s8 (top) and SLy5s1 parametrizations. The color of the lines indicates the expectation value of $\langle \hat{j}_z \rangle$ for the respective single-particle state: solid (dashed) lines correspond to levels of positive (negative) parity. The respective Fermi energies of protons and neutrons are drawn as dash-dotted black lines.

deformation for all nuclei in this region of the chart of nuclei, as exemplified already by Fig. 12.

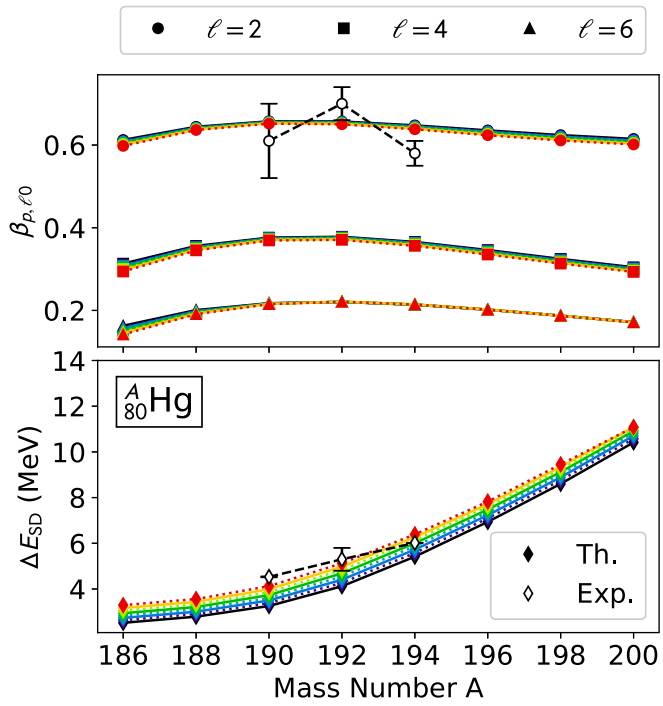

FIG. 15. Excitation energy $\Delta E_{\rm SD}$ with respect to the ground state and multipole deformations $\beta_{\ell 0}$ of the proton distribution of the superdeformed minimum for the even-even Hg isotopes as indicated and compared with experimental data where available (see text and Table III). The same color code as in Fig. 2 is used.

The excitation energy of the SD minimum of ^{194}Hg has been studied earlier with traditional parametrizations of the Skyrme EDF in Refs. [13,76]. The range of values found is larger than the one covered by the SLy5sX parametrizations.

We mention in passing that the appearance of the prolate ND minimum at $\beta_{20} \approx 0.3$ is associated with a ND prolate deformed band observed for isotopes with $N \approx 104$. Its excitation energy is notoriously difficult to describe [77–79]. In this respect, a very delicate observable is the odd-even staggering of charge radii of Hg isotopes between ^{180}Hg and ^{186}Hg, for which the prolate minimum remains an excited state for even-even nuclei, but becomes the ground state for the odd-A isotopes in between [62]. Among the parametrizations discussed here, this behavior is best, although not perfectly, described by the parametrizations with low $a_{\rm surf}$ up to SLy5s4 [62].

For the even-even nuclei whose energy curves are shown in Fig. 13, the actual values of the excitation energies of the SD minimum and corresponding proton deformation parameters are summarized in Fig. 15 for all eight parametrizations. A smaller value of $a_{\rm surf}$ systematically yields a smaller excitation energy. The deformation parameters are very similar with only small variations. There is the trend that parametrizations with lower $a_{\rm surf}$ produce slightly larger β_{20} than the parametrizations with higher $a_{\rm surf}$. For β_{40} and β_{60}, however, there is no such general trend.

Figure 15 also shows experimental data where available. Their detailed comparison with calculated values is provided

TABLE III. Charge quadrupole deformation $\beta_{2,p}$ and excitation energies $\Delta E_{\rm SD}$ (in MeV) of the superdeformed minima of Hg isotopes as indicated. Experimental data on the $\beta_{2,p}$ are taken from [80], whereas the estimates for $\Delta E_{\rm SD}$ are taken from [75] (^{190}Hg), [72] (^{192}Hg), and [70] (^{194}Hg; the authors do not provide an estimate of the error bar).

	^{190}Hg		^{192}Hg		^{194}Hg	
	$\beta_{2,p}$	$\Delta E_{\rm SD}$	$\beta_{2,p}$	$\Delta E_{\rm SD}$	$\beta_{2,p}$	$\Delta E_{\rm SD}$
SLy5s8	0.65	4.12	0.65	5.12	0.64	6.39
SLy5s7	0.65	3.99	0.65	4.98	0.64	6.27
SLy5s6	0.65	3.86	0.65	4.83	0.64	6.14
SLy5s5	0.65	3.73	0.65	4.69	0.64	6.01
SLy5s4	0.66	3.61	0.65	4.55	0.64	5.87
SLy5s3	0.66	3.50	0.66	4.41	0.64	5.73
SLy5s2	0.66	3.38	0.66	4.27	0.65	5.58
SLy5s1	0.66	3.26	0.66	4.12	0.65	5.42
Expt.	0.61(9)	4.53(2)	0.70(4)	5.3(5)	0.58(3)	6.017

by Table III. As already mentioned, the SD bands decay out to ND states at finite spin, such that the band head remains unobserved. The charge quadrupole moments are taken from the compilation of Ref. [80] and were each obtained from transition quadrupole moments averaged over several transitions between excited states in the yrast SD band. The excitation energies are estimated from γ-ray energies of transitions linking SD and ND states and subsequent extrapolation of the SD band to zero spin. For ^{190}Hg and ^{194}Hg, the latter has been achieved following discrete transitions [70,75], whereas the estimate for ^{192}Hg stems from a statistical analysis of a quasicontinuous spectrum [72].

For all three nuclei and all parametrizations, the calculated $\beta_{2,p}$ are almost identical and agree well, within error bars, with the empirical values with the exception of ^{194}Hg for which it is slightly overestimated. The excitation energy $\Delta E_{\rm SD}$, however, is less well described. First, the calculated values increase too quickly with N, and second, their values are better described for the parametrizations with large $a_{\rm surf}$, which has to be contrasted with the discussion of the fission barriers of ^{180}Hg, ^{226}Ra, and ^{240}Pu above, for which the barriers were best described by the parametrizations with lowest $a_{\rm surf}$. This, however, might be a trivial consequence of the slope of the $\Delta E_{\rm SD}$ being incorrect as a function of N.

The same overall pattern is also found when looking to such data for the adjacent even-even $^{192-196}$Pb isotopes; see Fig. 16 and Table IV. The calculated quadrupole moments are near identical for all parametrizations and nuclei and agree well with data, whereas the excitation energy $\Delta E_{\rm SD}$ increases much too quickly with N. As a consequence, the data for ^{192}Pb are best described with a parametrization with large $a_{\rm surf}$, whereas for ^{196}Pb a low $a_{\rm surf}$ is needed, with ^{194}Pb falling in between.

A possible incorrect trend in the surface symmetry energy coefficient $a_{\rm ssym}$ is not likely to be the explanation of the wrong trend of excitation energies. First of all, the deviation from experiment changes too quickly with N. Second, as argued when comparing barrier heights of ^{180}Hg, ^{226}Ra, and ^{240}Pu, the isospin dependence of the surface energy has probably to be changed in the opposite direction, which would make the disagreement with data for the SD minima in the $A \approx 190$ region even worse.

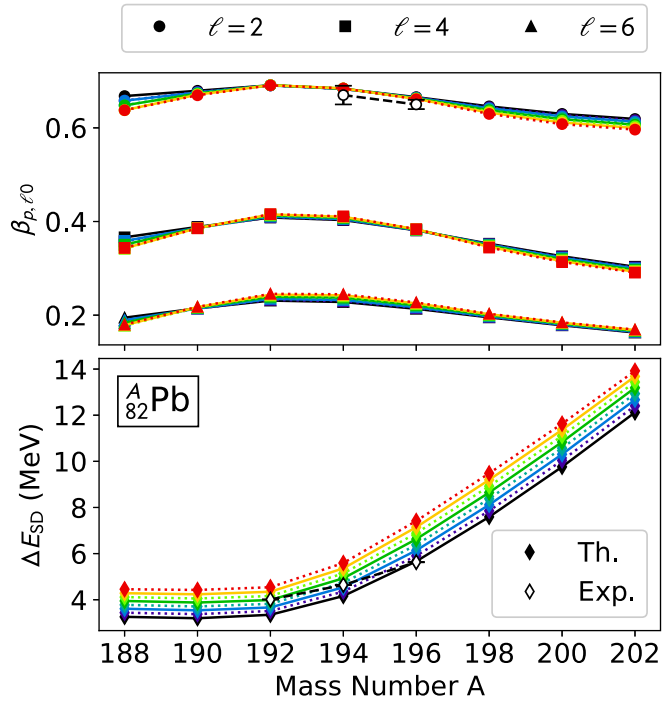

FIG. 16. Same as Fig. 15, but for Pb isotopes (see also Table IV).

A more likely explanation for the incorrect description of the slope of the $\Delta E_{\rm SD}$ are shell effects, that probably are not only incorrect in total size but also isotopic dependence. As argued above, the net shell effects are not the same for all parametrizations. The question of which one describes the shell structure best is difficult to answer from the material analyzed here and therefore beyond the scope of our study. There are, however, many indications that a satisfactory simultaneous description of nuclear bulk properties and shell structure

TABLE IV. Same as Table III, but for the Pb isotopes as indicated. Experimental data for $\beta_{2,p}$ are taken again from [80], whereas estimates for $\Delta E_{\rm SD}$ are taken from [73] (^{192}Pb), [71] (^{194}Pb), and [74] (^{196}Pb).

	^{192}Pb		^{194}Pb		^{196}Pb	
	$\beta_{2,p}$	$\Delta E_{\rm SD}$	$\beta_{2,p}$	$\Delta E_{\rm SD}$	$\beta_{2,p}$	$\Delta E_{\rm SD}$
SLy5s8	0.69	4.52	0.68	5.58	0.66	7.41
SLy5s7	0.69	4.30	0.68	5.35	0.66	7.14
SLy5s6	0.69	3.11	0.68	5.13	0.66	6.88
SLy5s5	0.69	2.96	0.68	4.92	0.66	6.62
SLy5s4	0.69	2.80	0.68	4.72	0.66	6.37
SLy5s3	0.69	2.65	0.68	4.53	0.66	6.13
SLy5s2	0.69	2.49	0.68	4.34	0.66	5.90
SLy5s1	0.69	2.34	0.68	4.15	0.67	5.66
Expt.		4.01	0.67(2)	4.64	0.65(1)	5.63(1)

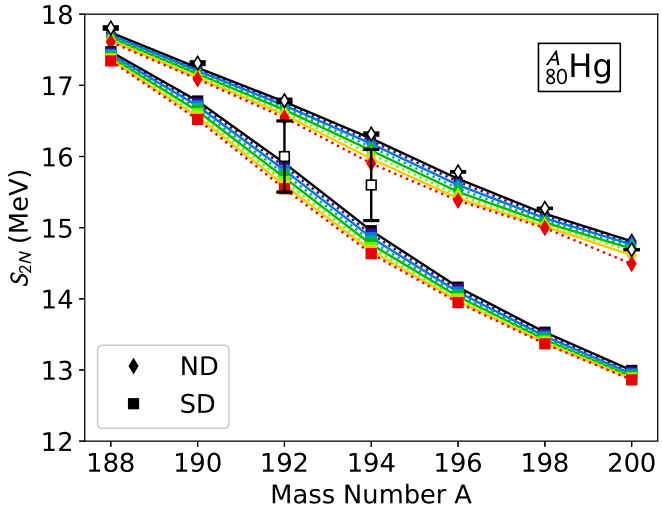

FIG. 17. Two-neutron separation energies S_{2n} of ground states and superdeformed states of neutron-deficient Hg isotopes as indicated using the same color code as in Fig. 2 for the calculated values. Experimental data are represented by open diamonds. For ground states they are taken from [84], for SD states from [75].

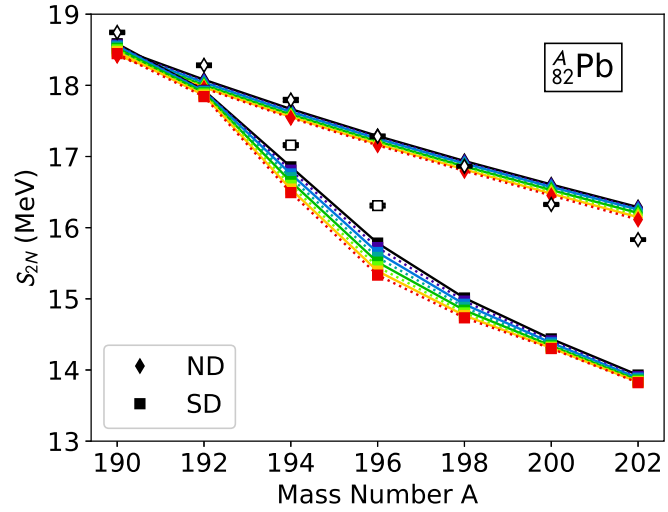

FIG. 18. Same as Fig. 17, but for Pb isotopes.

cannot be achieved with the presently used functional form of the nuclear EDF [17,20,24,81,82].

A discussion of the excitation energies of the SD band heads in the $A \approx 190$ region calculated with a large number of traditional parametrizations of the Skyrme EDF can be found in Ref. [13]. Results shown there indicate that the too quick increase of calculated $\Delta E_{\rm SD}$ values is a virtually universal feature of existing Skyrme interactions, although with differences in magnitude.

The slope of the excitation energies can also be analyzed through the two-neutron separation energy calculated between SD minima,

$$\begin{aligned} &S_{2n,\rm SD}(N,Z) \\ &\quad = E_{\rm SD}(N-2,Z) - E_{\rm SD}(N,Z) \\ &\quad = [E(N-2,Z) + \Delta E_{\rm SD}(N-2,Z)] \\ &\qquad - [E(N,Z) + \Delta E_{\rm SD}(N,Z)] \\ &\quad = S_{2n}(N,Z) + \Delta E_{\rm SD}(N-2,Z) - \Delta E_{\rm SD}(N,Z), \end{aligned} \quad (18)$$

where $\Delta E_{\rm SD}(N,Z)$ is the (positive) excitation energy of the SD minimum and $E(N,Z)$ the (negative) binding energy of the nuclide (N,Z). This quantity has been discussed earlier in Refs. [75,83]. Results for the $S_{2n,SD}(N,Z)$ of neutron-deficient Hg and Pb isotopes are compared with the conventional two-neutron separation energies between the ground states $S_{2n}(N,Z)$ and experimental data for both where available in Figs. 17 and 18.

The authors of Ref. [75] have argued that, compared to the two-particle separation energies of the respective ground states, "Naively, one might expect a reduction in both S_{2n} and S_{2p} at superdeformation, since both the binding energies per nucleon and the Coulomb barrier are lower." This, however, is a fallacy. First of all, if the SD states were all at constant excitation energy, then it is obvious that their two-particle separation energies would be identical to those of the ground states irrespective of what the E/A and Coulomb barrier are, as the latter are reduced for both nuclei entering the calculation of the separation energy. Second, if the S_{2n} of SD states were systematically smaller than those of ND states in a given isotopic chain, $S_{2n,\rm SD}(N,Z) < S_{2n}(N,Z)$, then Eq. (18) implies that the excitation energy of the SD states would always systematically increase with N, i.e., $\Delta E_{\rm SD}(N-2,Z) < \Delta E_{\rm SD}(N,Z)$. While the latter is indeed the case for the few $A \approx 190$ isotopes for which there are data, the systematics of data across the entire nuclear chart does not follow such a rule.

Irregularities in the systematics of two-nucleon separation energies can either indicate a gap in the single-particle spectrum or a large change in correlations [85], such as, for example, a large change in deformation.

As can be seen from Figs. 17 and 18, all SLy5sX give a fair description of the S_{2n} of the ground states in both isotopic chains. For Pb isotopes, the calculated S_{2n} do not fall off with exactly the same slope as the data, though. Differences between the parametrizations are very small in both slope and offset, which in view of their systematically different nuclear matter properties, see Table I, could not necessarily be expected. This point is analyzed further in Sec. IV F below. Similarly, differences between the $S_{2n,\rm SD}(N,Z)$ calculated with different parametrizations remain small, with an offset between the curves that is nearly identical to the one between the S_{2n}. In the region around $A \simeq 194$, the $S_{2n,\rm SD}$ are smaller than the S_{2n} and also falling off much quicker. For smaller mass numbers, the curves approach each other and become parallel. This behavior is simply a consequence of the up-bend of the $\Delta E_{\rm SD}$ with increasing mass in both isotopic chains as illustrated by Figs. 15 and 16.

The drop of the $S_{2n,\rm SD}$ of Pb isotopes when going from ^{194}Pb to ^{196}Pb is also reasonably described, although the overall size of the $S_{2n,\rm SD}$ is underestimated. Comparison with data for the Hg isotopes is compromised by their large error bars, but their values are also tentatively underestimated. In both cases, this is a direct consequence of the too large up-bend of the calculated $\Delta E_{\rm SD}$.

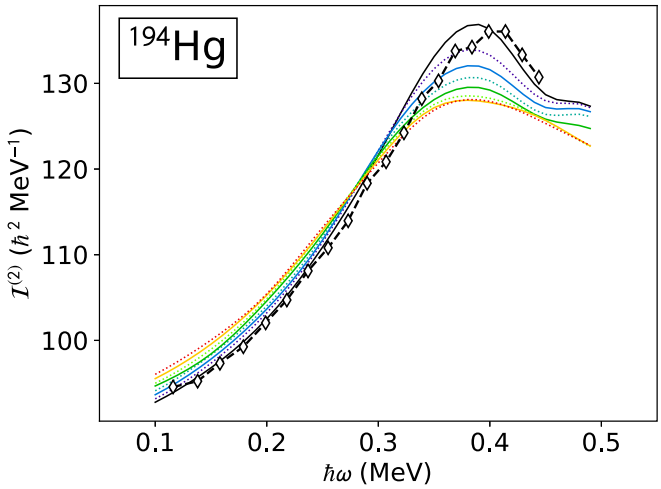

FIG. 19. Dynamical moment of inertia $\mathcal{I}^{(2)}$ of the superdeformed band in ^{194}Hg as a function of cranking frequency $\hbar\omega$ for the SLy5sX parametrizations indicated by the same color code as in Fig. 2. The white diamonds represent experimental data for the yrast SD-1 band taken from Ref. [80].

E. Superdeformed rotational bands

The properties of the 0^+ band heads of the SD yrast bands are obtained from extrapolation. More direct experimental information on SD states in the $A \approx 190$ region is provided by the rotational bands. Figure 19 displays the dynamical moment of inertia,

$$\mathcal{I}^{(2)} \equiv \left(\frac{d^2E}{dJ^2}\right)^{-1}, \tag{19}$$

of the yrast SD-1 band of ^{194}Hg as a function of rotational frequency ω,

$$\omega \equiv \frac{dE}{dJ}, \tag{20}$$

as obtained from cranked HFB calculations assuming triaxial shapes as described in Refs. [21,27,28]. In such calculations one minimizes the Routhian,

$$R = E - \omega_{\rm th}\langle \hat{J}_z\rangle. \tag{21}$$

The constraint on the expectation value of the z component of angular momentum breaks intrinsic time-reversal invariance, such that the time-odd terms of Eq. (3) contribute to the EDF and the single-particle Hamiltonian. The calculations described here have been performed using a linear constraint with fixed $\omega_{\rm th}$, the value of which is also used to draw the curves in Fig. 19.

For an even-even nucleus and $\Delta J = 2\,\hbar$ transitions, the experimental values for ω and $\mathcal{I}^{(2)}$ are calculated from data provided by Ref. [80] with the help of finite difference formulas [86],

$$\hbar\omega_{\rm exp} = \frac{1}{4}[E_\gamma(J+2\to J) + E_\gamma(J\to J-2)], \tag{22}$$

$$\mathcal{I}^{(2)}_{\rm exp} = \frac{4}{E_\gamma(J+2\to J) - E_\gamma(J\to J-2)}, \tag{23}$$

where E_γ is the energy of the γ ray emitted in the transition from the level with J to the level with $J-2$. Both can be determined without knowing the angular momentum J of the states involved as is often the case for SD rotational bands.

All SLy5sX parametrizations give a fair description of the data; in particular those with the smallest surface coefficients perform as well as the best parametrizations identified in previous applications [21,87]. The differences between the parametrizations observed here are in general smaller in size than the ones obtained when varying the strength of the pairing interaction or the not well-constrained time-odd terms of the EDF [21], two ingredients of the EDF that are much smaller in magnitude than the surface energy.

There are small systematic differences between the parametrizations; at low frequency, SLy5s8 exhibits the largest moment of inertia, while at higher frequencies the ordering is reversed and SLy5s1 has the largest value of $\mathcal{I}^{(2)}$. The difference between the parametrizations is largest around $\hbar\omega \approx 0.38$ MeV, where the moment of inertia first plateaus and later drops off. In this region, SLy5s1 follows the data most closely. This, however, is not related to any difference in deformation between the parametrizations, which become even closer with increasing J. In fact, this saturation of the rotational band in this region is usually associated with the alignment of neutron intruder orbitals [87], which are at a slightly different position for each Sly5sX because of the systematic differences in spin-orbit strength; see the discussion of Fig. 14.

F. Isotopic trends of ground states

In the discussion of Figs. 17 and 18 we have seen that the SLy5sX parametrizations give similar results for two-neutron separation energies. In view of the systematic differences between INM properties discussed in Sec. II B this might come as a surprise. Indeed, as listed in Table I, the symmetry energy coefficient $a_{\rm sym}$ steadily changes from 31.43 MeV for SLy5s1 to 32.64 MeV for SLy5s8, which has no significant impact on the S_{2n} of neutron-deficient Hg and Pb isotopes.

The same result is found when looking at the S_{2n} along the chain of Sn isotopes; Fig. 20. The curves for the various parametrizations almost everywhere fall on top of each other, with the exception of nuclei just below the $N = 82$ shell closure and the least bound ones close to the neutron drip line. The global trend of the data is well described, including the size of the jump at $N = 82$.

For comparison, in Fig. 20 we also show the two-neutron separation energy obtained as

$$S_{2n,\rm LDM}(N,Z) \equiv -2\frac{dE_{\rm LDM}(N,Z)}{dN} \tag{24}$$

from the LDM energy (6) calculated from the INM and SINM properties of the SLy5sX parametrizations. Again, the curves almost perfectly fall on top of each other. Qualitatively, the same is found when looking at the two-proton separation energies of $N = 82$ isotones; cf. Fig. 21. Several comments on these results are in order:

(i) While the evolution of observables along isotopic and isotonic chains is frequently used for the analysis of the

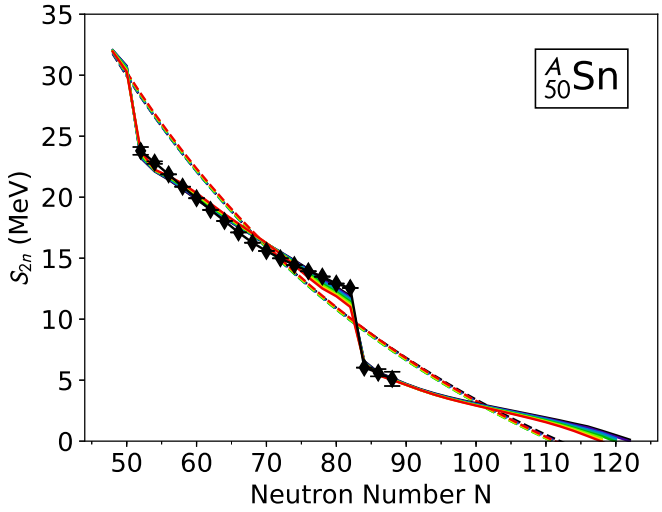

FIG. 20. Two-neutron separation energies S_{2n} of even-even Sn isotopes. Solid lines are results from HFB calculations with the parametrizations as indicated, whereas dotted lines are the $S_{2n,\mathrm{LDM}}$ calculated through Eq. (24) from LDM models with same INM and SINM parameters as the SLy5sX. Experimental data are taken from [84].

impact of isovector terms, which scale with the square of the asymmetry $I = N - Z$, the mass number $A = N + Z$ also changes at the same time, such that isoscalar and isovector effects are inevitably intertwined.

(ii) For the SLy5sX parametrizations, both the isoscalar and isovector INM parameters are changing as a function of the constraint on a_{surf}; cf. Table I. The coefficients a_{vol} and a_{sym} of the dominating contributions to the LDM energy change in opposite direction. Combined with the changes in the surface terms, the net effect is that the separation energies are almost unchanged when going from one SLy5sX parametrization to another. This would be different if all other LDM parameters were fixed and only a_{surf} varied.

(iii) While the HFB results for the S_{2n} and S_{2p} oscillate around the LDM results, at no point do the HFB values (or the experimental data, for that matter) follow the slope of the LDM values.

Indeed, the two-neutron separation energy $S_{2n} \approx -2\lambda_n$ approximates the negative of twice the Fermi energy of neutrons, and similar for protons. As a consequence, the overall trend of the microscopically calculated S_{2n} and S_{2p} is determined by the position of single-particle levels and the correlations from pairing and deformation modes. These are very similar for all SLy5sX parametrizations except for the isotopes just below ^{132}Sn, where the position of the $h_{11/2^-}$ intruder neutron level depends strongly on the parametrization, very similar to what has been found for the proton $h_{11/2^-}$ level of ^{188}Hg in Fig. 14.

The impact of the variations in a_{vol} and a_{sym} can only be seen when looking at observables as a function of A at constant I and as a function of I at constant A, respectively. For example, the softening of E/A with increasing mass number when going from SLy5s1 to SLy5s8 visible in Fig. 8 is a consequence of the increase of a_{vol} from -15.77 to -16.10 MeV.

This has some visible influence on the global trend of mass residuals of heavy nuclei. Changing a_{vol} by as little as 0.1 MeV while keeping all other LDM coefficients constant changes the binding energy of ^{208}Pb by 20.8 MeV and that of ^{240}Pu by 24 MeV. Like many other widely used parametrizations of the Syrme EDF, all SLy5sX underbind actinide nuclei, but to a different degree. Going from SLy5s8 to SLy5s1, the underbinding of ^{240}Pu increases from about 6 MeV to almost 16 MeV, which is close to what can be naively expected from the change in a_{vol}, provided that ^{208}Pb has the same binding energy in both cases. Because of the change of all terms in Skyrme EDF (2) and the corresponding LDM energy (6), however, this estimate is less reliable than it may seem.

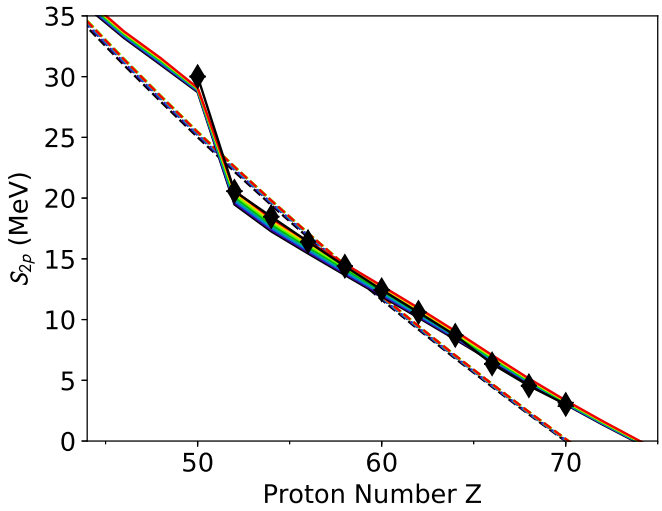

FIG. 21. Two-proton separation energies S_{2p} of even-even $N = 82$ isotones represented in the same way as the S_{2n} of Sn isotopes in Fig. 20.

G. Shape coexistence at normal deformation

1. *Shape coexistence in* ^{186}Pb

Like the neutron-deficient Hg isotopes, Pb isotopes in the $A \approx 180$ region exhibit shape coexistence at normal deformation. A spectacular example is given by ^{186}Pb, for which the three lowest-lying states are 0^+ states interpreted as spherical, prolate, and oblate shapes [88]. The ground state is associated with a spherical shape, and the 0^+ states at 536(21) and 655(21) keV are oblate and prolate configurations. Correlations do of course lead to a mixture of the pure configurations.

This behavior is qualitatively reproduced by all SLy5sX parametrizations; see Fig. 22. The excitation energy of the deformed minima, however, is largely overestimated. The situation can be improved by reducing the pairing strength [89], although this would in turn degrade the description of other observables, most notably the dynamical moment of inertia of the SD band of ^{194}Hg of Fig. 19.

In any event, on the scale of the figure, changing a_{surf} has no visible impact on the deformation around the spherical point up to oblate deformations well beyond the minimum, which is a consequence of a simultaneous change in shell

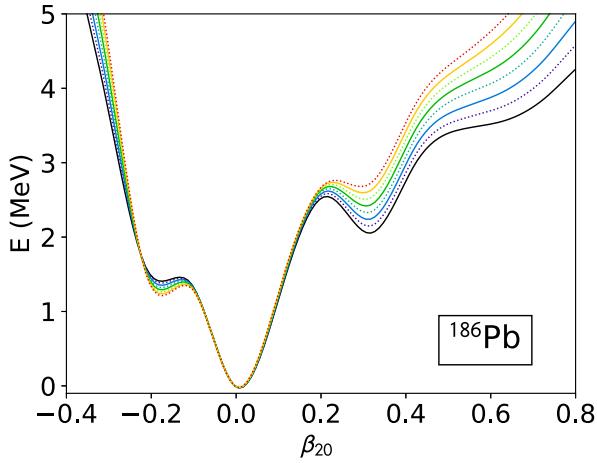

FIG. 22. Deformation energy of ^{186}Pb as a function of the axial mass quadrupole deformation β_{20} for the SLy5sX parametrizations indicated with the same color code as in Fig. 2.

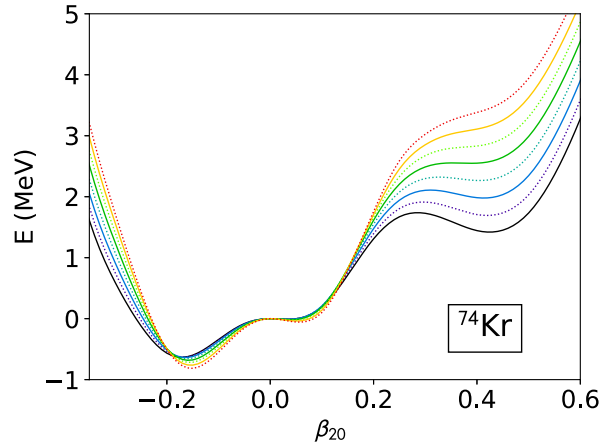

FIG. 23. Same as Fig. 22, but for ^{74}Kr.

effects as deduced already from Figs. 6, 7, and 12 for adjacent nuclei. By contrast, reducing $a_{\rm surf}$ slightly lowers the prolate minimum and makes it more pronounced. The impact of changing $a_{\rm surf}$, however, only becomes clearly visible at larger deformation than the one of the coexisting states. Altogether, this indicates that the surface energy coefficient is not the most relevant degree of freedom for the fine-tuning of shape-coexisting states in neutron-deficient Pb isotopes. Modifying the pairing strength or changing the shell structure by variation of the tensor terms has a much larger effect [20] on the energy differences between the minima.[2]

It has to be noted that these states are much better described in beyond-mean calculations that combine projection on angular momentum and particle number with configuration mixing in a generator coordinate method (GCM) using parametrizations that, at the mean-field level, perform similarly to the SLy5sX with low $a_{\rm surf}$ [89–91]. This indicates that a mean-field description of shape coexistence in this mass region might not be sufficient, as each of the three low-lying 0^+ states gains a quite different amount of correlation energy.

2. *Shape coexistence in* ^{74}Kr

Another region of the nuclear chart for which detailed data on shape coexistence are available is the neutron-deficient Kr region. As an example, Fig. 23 shows the deformation energy curve for axial states of ^{74}Kr. At large deformation $|\beta_{20}| \gtrsim 0.25$, the curves behave as expected from the $a_{\rm surf}$ of each parametrization, but at small deformations their order is inverted: SLy5s8 gives a softer energy curve around the spherical point than SLy5s1. The reason is again the difference in spin-orbit interaction, which is weaker for the former than for the latter. The resulting small changes in shell structure then increase or decrease the binding energy for near-spherical shapes relative to those at larger deformation. What appears as a prolate shoulder in calculations with SLy5s8 becomes a pronounced low-lying excited minimum with SLy5s1.

Electromagnetic transition moments between the low-lying states, however, indicate that the ground-state band is dominated by prolate shapes with $\beta_2 \approx 0.4$ [92], whereas an excited band is mainly built from oblate shapes. From this follows that none of the SLy5sX describes the correct relative position of the minima. Extrapolating the trend of the SLy5sX, $a_{\rm surf}$ had to be reduced by more than 1 MeV below the value of SLy5s1 in order to get the correct order of the minima. Such parametrization would have unrealistic properties for fission barriers of actinides. However, for this nucleus that is almost on the $N = Z$ line, the combined reduction of $a_{\rm surf}$ by about 0.6 MeV and (for this nucleus irrelevant) increase of $a_{\rm ssym}$ proposed in Sec. IV B 4 in order to obtain simultaneously the fission barrier heights of ^{180}Hg and ^{240}Pu would nevertheless improve on the situation.

A low value of $a_{\rm surf}$ is most probably a necessary ingredient for the quantitative description of shape coexistence in this region of the chart of nuclei, but it can again be argued that other aspects of the parametrizations such as shell structure and pairing correlations are of at least equal importance and require further fine-tuning in order to describe the energy difference between the minima in a mean-field calculation.

Like for ^{186}Pb, beyond-mean-field calculations based on parametrizations that give a similar energy surface as SLy5s1 give an excellent description of low-lying states in this nucleus [93–95], hinting again at the possible insufficiency of mean-field calculations to quantitatively describe shape coexistence phenomena at normal deformation.

3. *Structure of* ^{110}Zr

Nuclei in the Zr region exhibit a rich and quickly evolving structure, that is notoriously difficult to describe in all details by mean-field models [20]. Data suggest that ^{80}Zr is prolate deformed, while ^{90}Zr is quasidoubly magic. The heavier ^{96}Zr is usually interpreted as a spherical nucleus with low-lying collectively deformed states, while adding four neutrons leads to the well prolate deformed ^{100}Zr. A model-dependent

[2]According to the tables provided by Ref. [8], with $a_{\rm surf}^{\rm MTF} \simeq 19.0 \pm 0.25$ MeV, the surface energy coefficients of the Tij parametrizations used in Ref. [20] are all on the upper end of the scale covered by the SLy5sX.

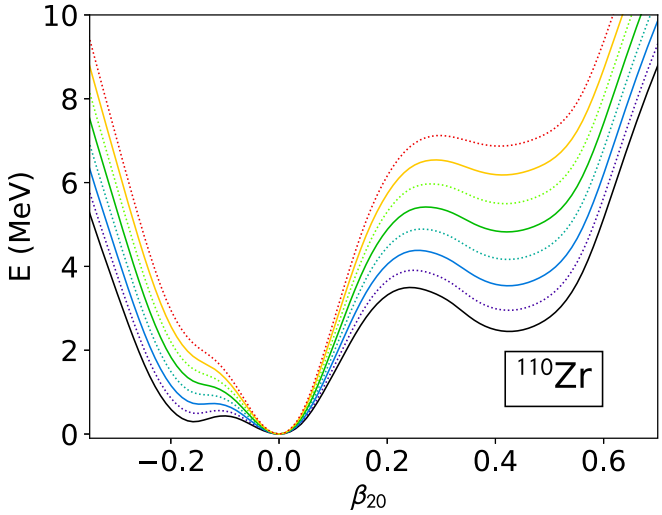

FIG. 24. Same as Fig. 22, but for ^{110}Zr.

analysis of recent data suggests that the even heavier neutron-rich ^{110}Zr is γ-soft with a preference for prolate shapes [96].

The axial energy curves as obtained with the SLy5sX parametrizations for this last nucleus are shown in Fig. 24. Going from SLy5s8 to SLy5s1, the energy surface becomes softer, with an oblate minimum developing at $\beta_{20} \simeq -0.1$ that is lowered to 110 keV excitation energy for SLy5s1, while prolate states at $\beta_{20} \simeq 0.4$ are lowered by about 5 MeV. The absolute minimum, however, is spherical for all parametrizations, with the prolate states remaining at excitation energies of 2.34 MeV for SLy5s1 and up to 6.48 MeV for SLy5s8.

As can be seen from the energy surfaces in the full β-γ plane, Fig. 25, the prolate structure is in fact a saddle for all SLy5sX parametrizations. The D1S parametrization of the Gogny force gives an energy surface that is very similar to the one of SLy5s1. As has been demonstrated in Ref. [96], a modified D1S with increased strength of the spin-orbit interaction (from a value slightly larger than the one for SLy5s1 to an even larger one) significantly improves the description of the available spectroscopic data. The main effects of this change are that the spherical state is slightly pushed up and that the global minimum becomes prolate. A similar effect can be obtained by a modification of tensor terms [20], although this might degrade properties of other nuclei.

Without discussing them in detail, we can mention that the changes of the deformation energy curves of ^{80}Zr, ^{96}Zr, and ^{100}Zr are similar to what we find for ^{74}Kr and ^{110}Zr: changing $a_{\rm surf}$ shifts very deformed prolate and oblate states, but does not affect much the shape of the energy curves for $|\beta_{20}| \lesssim 0.15$, nor alter the relative order of the coexisting minima. Both ^{80}Zr and ^{100}Zr have a spherical ground state for all SLy5sX.

Altogether, this indicates that the value of the surface energy coefficient $a_{\rm surf}$ is an important ingredient for the correct description of the evolution of shapes in the Zr region, with a preference for low values like the one of SLy5s1. Other ingredients of the model such as details of shell structure have to be precisely controlled as well, however, and modifications of the SLy5sX in that respect are necessary.

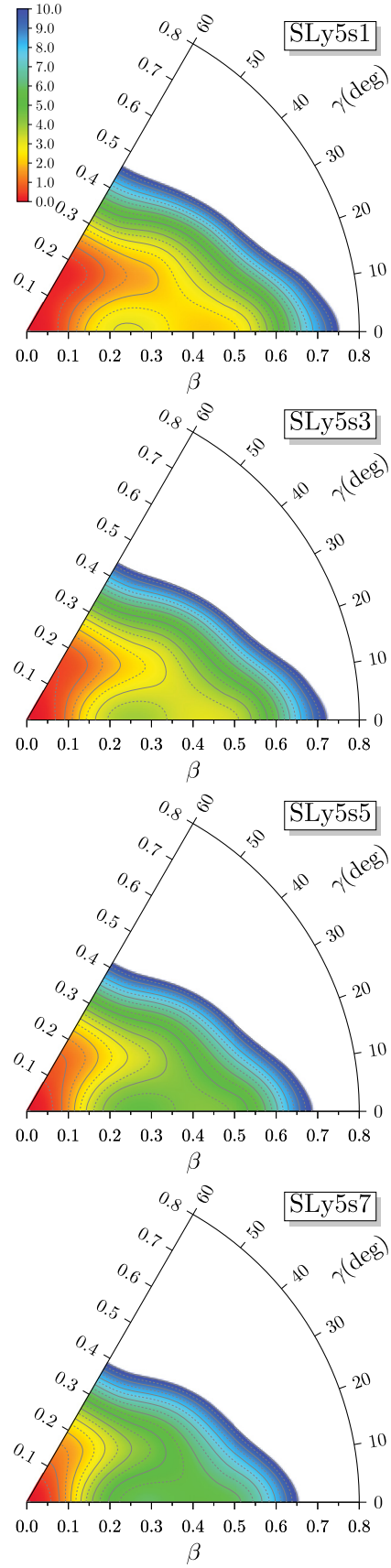

FIG. 25. Deformation energy surfaces in the β-γ plane of ^{110}Zr obtained with the SLy5sX parametrizations as indicated.

H. Exotic deformation

In the previous sections we discussed the impact of $a_{\rm surf}$ on the ground and excited states whose shapes are dominated by quadrupole deformations. Indeed, deformations of even multipolarity, $\beta_2, \beta_4, \beta_6, \ldots$, are relevant in virtually every region of the nuclear chart. Moments of odd multipolarity, in particular β_{30} and β_{32}, are in general less important and in most cases take a zero value for ground states calculated at the mean-field level. Nevertheless, there are specific regions where this is not the case. Axial octupole deformation β_{30} plays a role for nuclei around ^{226}Ra, whose fission barrier has already been discussed in Sec. IV B, or the region around ^{144}Ba [97]. The possible role of dominant β_{32} deformations in specific regions of the chart of nuclei is also discussed in the literature [98].

The appearance of regions of octupole deformation can be associated with the presence of single-particle levels of opposite parity near the Fermi energy that are mixed by the octupole deformation in such a way that the density of levels near the Fermi energy is significantly reduced.

Unlike quadrupole deformation of the intrinsic states, that manifests itself through rotational bands and that can be directly measured for excited states with angular momentum larger than 1/2, indications for octupole deformation are always indirect: the expectation value of a parity-odd operator is zero in experiment. The presence of static intrinsic β_{30} deformation can be deduced from rotational bands with a characteristic pattern of levels with alternating parity that exhibit strong $E1$ and $E3$ transitions [99,100].

Like the calculations of fission barriers in Sec. IV B the calculations discussed in this subsection have been carried out by breaking parity, but conserving z signature and y time simplex of the single-particle states, which introduces two plane reflection symmetries of the local density $\rho(\mathbf{r})$ [38].

1. Axial octupole deformation

As a first example, we consider the medium-mass nucleus ^{144}Ba, for which recent experimental data from Coulomb excitation indicate static octupole deformation [97]. Figure 26 shows the deformation energy of this nucleus as a function of the axial octupole moment β_{30} with diamonds indicating the position of the respective minima. As these configurations are also quadrupole deformed, $\beta_{30} = 0$ corresponds to an axial prolate deformed saddle point of the complete deformation energy surface. The octupole deformation of the minimum, which is quite appreciable for SLy5s1 with $\beta_{30} \sim 0.15$, diminishes with increasing $a_{\rm surf}$. Simultaneously, the minimum becomes more shallow, until it vanishes for SLy5s7 and SLy5s8: for these, the mean-field minimum is reflection symmetric.

Assuming a rigid axial rotor, the reduced $E2$ matrix element $\langle 2^+||\mathcal{M}(E2)||0^+\rangle = 1.024^{+17}_{-22}\,e$b obtained in Ref. [97] can be identified with $\langle Q_{20,p}\rangle$. From this, one obtains a value of $\beta_{2,p} = 0.197^{+3}_{-4}$ for the quadrupole deformation of the protons defined through Eq. (17). This value compares very well with the calculated values for $\beta_{2,p}$ that fall into the range between 0.198 (SLy5s1) and 0.196 (SLy5s8).

Identifying the measured reduced $E3$ matrix element $\langle 3^-||\mathcal{M}(E3)||0^+\rangle = 0.65^{+17}_{-23}\,e\text{b}^{3/2}$ along the same lines with $\langle Q_{30,p}\rangle$, Eq. (17) leads to a value of $\beta_{30,p} = 0.195^{+51}_{-69}$ for the proton octupole deformation. It is appreciably larger than the largest octupole deformation of about $\beta_{30,p} \simeq 0.1$ obtained in the calculations (for SLy5s1). As discussed in Ref. [97], the same underestimation of data is also found when comparing with published $\beta_{30,p}$ values from earlier calculations of ^{144}Ba with a large variety of EDFs.

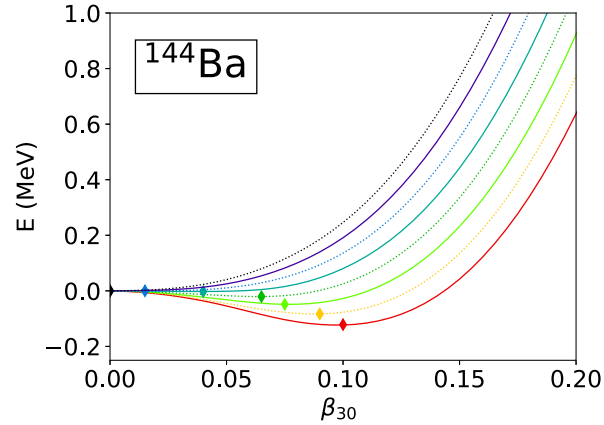

FIG. 26. Deformation energy of ^{144}Ba relative to the respective axial reflection-symmetric quadrupole-deformed saddle point as a function of β_{30} for the SLy5sX parametrizations indicated with the same color code as in Fig. 2. The minimum of each energy curve is marked by a filled diamond.

Extrapolating the behavior of the energy curves of Fig. 26 beyond the range covered by the SLy5sX, it is clear that the empirical octupole deformation cannot be reached through just further reduction of $a_{\rm surf}$. For SLy5s1, the energy gain with respect to the reflection-symmetric saddle is 200 keV, while for all other parametrizations the surface is even softer with respect to octupole deformation. This is to be contrasted with quadrupole deformation, which for this nucleus brings an energy gain of several MeV. The difference in scale makes octupole deformation more elusive and fragile than quadrupole deformation, and also more sensitive to details of shell structure and also pairing correlations.

Octupole correlations become more pronounced, however, when projecting the reflection-asymmetric mean-field states on parity [101], thereby improving the agreement with experiment [102] for this nucleus.

As an example from the $A \approx 220$ mass region, Fig. 27 shows the energy gain from reflection-asymmetric shape degrees of freedom, as well as the quadrupole and octupole deformations of the minimum, for even-even Th isotopes between ^{214}Th and ^{232}Th. As in some cases nonconstrained HFB+LN calculations did not converge to the minimum of the energy surfaces because of the nonvariational character of the LN procedure, the results were obtained from interpolation of energy surfaces constructed around the minimum. For ^{214}Th, ^{216}Th (both not shown), and ^{218}Th, the lowest mean-field configuration is in fact spherical because of the proximity to the $N = 126$ shell closure. From ^{220}Th onwards, octupole and quadrupole deformation set in simultaneously. For the transitional ^{220}Th, a very shallow octupole-deformed minimum is found for all parametrizations but SLy5s7 and

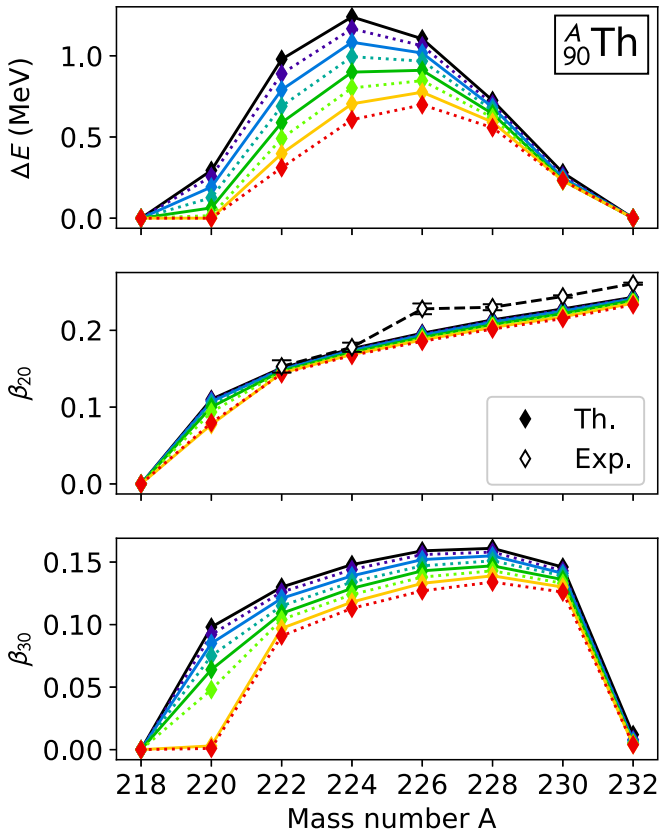

FIG. 27. Energy gain ΔE of the nuclear ground state from reflection-asymmetric shape degrees of freedom, as well as quadrupole and octupole deformation of even-even Th isotopes as obtained from calculations with the SLy5sX parametrizations and represented with the same color code as used in Fig. 2. Experimental data for charge quadrupole deformations $\beta_{20,p}$ taken from [103] and [104] (^{224}Th) are given for comparison.

SLy5s8, and that in the most favorable case of SLy5s1 is 294 keV below the reflection-symmetric saddle.

The heavier isotopes up to ^{228}Th exhibit a much more pronounced asymmetric minimum, with an energy gain of the order of 1 MeV for SLy5s1, which is significantly larger than what we found for ^{226}Ra and ^{144}Ba. Beyond ^{228}Th, the octupole deformation is quickly decreasing again, while the quadrupole deformation continues to grow. The size of octupole deformation is correlated to $a_{\rm surf}$: for all strongly octupole-deformed Th isotopes shown in Fig. 27 the value of β_{30} for the calculated minimum significantly decreases with increasing $a_{\rm surf}$. The values obtained with SLy5s8 are typically 30% smaller than those from SLy5s1. The same correlation with $a_{\rm surf}$ can also be found for the quadrupole deformation β_{20}, but on a much smaller scale that is not significant. With the exception of an anomaly for ^{226}Th, all SLy5sX describe very well the size and global trend of the experimental $\beta_{20,p}$.

From the available experimental information for rotational bands in these nuclei it has been concluded that the spectrum of ^{220}Th cannot be interpreted in terms of an octupole-deformed rigid rotor [105]. Alternating parity bands are observed starting from ^{222}Th onwards [106]. For ^{222}Th, ^{224}Th, and ^{226}Th, the pattern can be interpreted in terms of a rigid octupole rotor, whereas the data for ^{230}Th and ^{232}Th suggest that at low spin the octupole deformation is vibrational. The bands of the latter resemble the one of an octupole-deformed rotor only at higher spin, while ^{228}Th is transitional in between the two regimes [106]. Up to ^{232}Th, our findings are compatible with the data, keeping in mind that, like in the case of transitional quadrupole-deformed nuclei, it is not obvious to deduce how the particular spectroscopic features of ^{220}Th on the one hand and the vibrational character of ^{230}Th and ^{232}Th on the other hand should be reflected by their mean-field deformation energy surface. In any event, the very shallow minima found for these three nuclei (as indicated by their small energy gain) suggests that a mere mean-field calculation might not be sufficient to describe states in this nucleus. In particular the energy surfaces of ^{230}Th and ^{232}Th have a long leveled valley in β_{30} direction at almost constant β_{20} [107] that could indeed lead to large-amplitude octupole vibrations.

For the isotopes that can be interpreted in terms of a static octupole rotor, there are no available data for $B(E3)$ transitions to the ground state.[3]

Other forms and parametrizations of the nuclear EDF overall agree on the octupole deformation of Th isotopes in this mass region, but might differ in details [100]. In calculations using the D1S and D1N parametrizations of the Gogny force, the onset of octupole deformation in the mean-field ground states is also found for ^{220}Th, whereas for D1M the lightest octupole-deformed isotope is ^{222}Th [101]. The DD-PC1 and NL3 parametrizations of relativistic EDFs predict octupole deformation only beginning with ^{224}Th [109] or even ^{226}Th [110], respectively.

At the mean-field level, SLy5s1 with its low $a_{\rm surf}$ gives the most pronounced octupole deformation, which is also the parametrization that tends to agree best with the data discussed up to now. Further discussion of the structure of ^{222}Th, including its rotational band, as obtained from calculations with SLy5s1 can be found in Ref. [111]. A very detailed study of the structure of even and odd Th isotopes also using SLy5s1 will be presented elsewhere [107].

2. *Nonaxial octupole deformations*

In Sec. IV B, we saw that nonaxial octupole deformations β_{32} can lower the static fission path around the saddle point, as has been reported earlier, for example in Refs. [51,112].

The relevance of β_{32} for low-lying states at normal deformation was originally discussed to characterize cluster structures in light nuclei [113]. It is the leading deformation degree of freedom characterizing tetrahedral and octahedral shapes [98,114]. Similar to quadrupole deformation, such symmetries are predicted to give rise to substantial deformed shell gaps at specific particle numbers and, hence, might be present in nuclear ground states or excited states at low excitation energy.

[3]Putting the $B(E3, 0^+ \to 3^-)$ values of the *vibrational* ^{230}Th and ^{232}Th reported in Ref. [108] into the expression for $\beta_{30,p}$ of an octupole-deformed *rotor*, one obtains $\beta_{30,p} = 0.094(29)$ for ^{230}Th and $\beta_{30,p} = 0.085(28)$ for ^{232}Th, respectively.

In the expansion of the surface of a liquid drop along the lines of Eq. (10) that includes all spherical harmonics, octahedral shapes are characterized by finite α_{32}, $\alpha_{40} = -\sqrt{14/5}\,\alpha_{44}$, and $\alpha_{60} = \sqrt{2/7}\,\alpha_{64}$, with all other $\alpha_{\ell m}$ equal to zero up to $\ell = 6$ [114]. Note that such shape is also invariant under the tretrahedral point group [114]. For the same reasons that lead to a difference between α_{20} and β_{20} discussed above, however, the deformations $\beta_{\ell m}$ of Eq. (12) calculated from multipole moments are not equal to the $\alpha_{\ell m}$ such that the relations between the $\alpha_{\ell m}$ of same ℓ cannot be expected *a priori* to also hold exactly for the $\beta_{\ell m}$.

The neutron-rich ^{110}Zr is one of the the most detailed studied candidates for tetrahedral deformation [98,115–118]. Recent experimental evidence [96] has invalidated the prediction for the ground-state band, although excited bands could still exhibit tetrahedral or octahedral character.

Figure 28 shows the energy curve of ^{110}Zr as a function of β_{32}. The quadrupole deformations β_{20} and β_{22} are constrained to be zero, such that $\beta_{32} = 0$ corresponds to a spherical shape. Unlike all other calculations presented in this study, these were performed at the HF level neglecting pairing correlations. In HFB+LN calculations using the same pairing interaction as above, there is no deformed minimum for any of the SLy5sX; instead, the curves are slowly rising with β_{32}. By contrast, HF calculations yield a very shallow minimum for all SLy5sX. Like in the case of the axial octupole deformation of ^{144}Ba and the Th isotopes, with decreasing $a_{\rm surf}$ the minima become more pronounced in both width and depth.

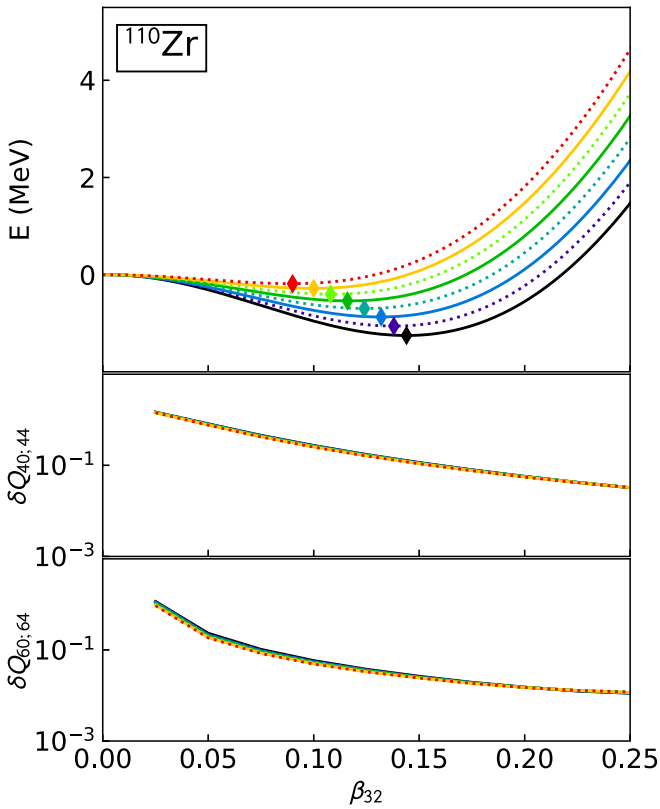

FIG. 28. Deformation energy of ^{110}Zr as a function of the nonaxial octupole deformation β_{32} from HF calculations without pairing correlations using the SLy5sX parametrizations as indicated. The lower panels show the absolute value of the relative deviation between higher-order multipole deformations defined as $\delta Q_{40:44} \equiv |(Q_{40} + \sqrt{14/5}\,Q_{44})/Q_{40}|$ and $\delta Q_{60:64} \equiv |(Q_{60} - \sqrt{2/7}\,Q_{64})/Q_{60}|$ that characterize the closeness to an octahedral solution (see text). All configurations along the curve have been constrained to have $\beta_{20} = \beta_{22} = 0$ in order to prevent the code from converging to the lower-lying quadrupole-deformed minimum of the energy surfaces displayed in Fig. 25.

The lower two panels show the relative deviation of $-\sqrt{14/5}\,\beta_{44}$ from β_{40} and of $\sqrt{2/7}\,\beta_{64}$ from β_{60}. The relations between the surface moments $\alpha_{\ell m}$ mentioned above are reasonably well respected. Up to numerical noise, the other nonconstrained low-order deformations take a value of zero, $\beta_{30} = \beta_{42} = \beta_{5\ell} = \beta_{62} = \beta_{66}$, indicating that the shapes along the energy curve exhibit indeed octahedral symmetry. For SLy5s1, the actual multipole deformations at the minimum are $\beta_{32} = 0.15$, $\beta_{40} = -0.027$, $\beta_{44} = 0.014$, $\beta_{60} = 0.019$, and $\beta_{64} = 0.037$.

V. CONCLUSIONS

We have studied the correlation of the value of the surface energy coefficient $a_{\rm surf}$ with observables characterizing deformation phenomena in atomic nuclei. To that end, we performed calculations with the recent SLy5sX parametrizations of the standard Skyrme EDF that were each adjusted within the same protocol with a constraint on a systematically varied value of $a_{\rm surf}$. Going from SLy5s1 with the lowest $a_{\rm surf}$ to SLy5s8 with the highest value covers the range of $a_{\rm surf}$ typically found for widely used Skyrme parametrizations.

Using a family of fits for which all other properties are as similar as possible is crucial for such study. This is particularly pertinent with regard to shell effects. Indeed, the complicated topography of deformation energy surfaces with multiple deformed minima and saddles in between is generated by shell effects, with the surface energy only providing a smooth background.

The main conclusions concerning the description of properties of finite nuclei that can be drawn are as follows:

(i) As expected, the deformation energy of highly deformed configurations is clearly correlated to $a_{\rm surf}$. For the saddle points of very wide fission barriers of heavy nuclei, the difference between what is obtained with SLy5s1 and SLy5s8 can amount to as much as 10 MeV.

(ii) The description of fission barrier heights of nuclei in the $A \approx 240$ actinide and neutron-deficient $A \approx 180$ Hg region improves dramatically when reducing $a_{\rm surf}$, with a clear preference for the SLy5s1 parametrization.

(iii) The performances of the SLy5sX for the barrier height of ^{240}Pu and ^{180}Hg, two nuclei with very different asymmetry I, are not the same. When the barrier height of ^{240}Pu is correctly described, then the one of ^{180}Hg is largely overestimated. One possible explanation is that the surface symmetry energy coefficient $a_{\rm ssym}$, which takes very similar values for all SLy5sX, needs fine-tuning too, such

that the effective surface energy coefficient $a_{\rm surf,eff}(I)$ decreases less quickly with asymmetry I. This, however, would require a further reduction of $a_{\rm surf}$ below the SLy5s1 value.

(iv) The clear correlation between barrier height and $a_{\rm surf}$ fades away when going to superheavy nuclei in the $Z \simeq 110$ region. These systems are characterized by a vanishing liquid-drop fission barrier, such that solely the details of shell structure determine the fission barrier. For these systems, all SLy5sX give very similar results.

(v) Results for the excitation energy of the superdeformed minimum of nuclei in the $A \approx 190$ region do not follow the same trends as the fission barrier heights: for some nuclei such as ^{190}Hg it is even underestimated by all SLy5sX parametrizations. This has to be contrasted with the fission barrier of ^{180}Hg, that is overestimated by all SLy5sX parametrizations, in particular those with high $a_{\rm surf}$. In general, the excitation energy of the superdeformed states increases too rapidly with asymmetry I. As the fission isomer of the much more asymmetric ^{240}Pu is reasonably described by the SLy5s1 parametrization that also fairly describes the barrier height, the difficulties to describe the known superdeformed states of Hg and Pb nuclei have to be a local particularity of the $A \approx 190$ region. The most likely explanation is that the modeling of these states is compromised by deficiencies in the description of shell effects and their dependence on N, Z, and deformation. Improvements of this aspect of nuclear EDFs could also slightly alter the conclusions about fission barrier heights drawn above, but are unlikely to be achievable within the present standard form of the Skyrme EDFs.

(vi) At normal deformation, the changes in surface energy when going from one SLy5sX parametrization to another are naturally smaller and also often masked by simultaneous small changes in shell effects, in particular for oblate states. The relative energy between coexisting minima is less strictly correlated to $a_{\rm surf}$ as is the case at larger deformation. None of the SLy5sX parametrizations provides a correct description of shape coexistence and shape evolution in the region of Kr and Zr isotopes at the mean-field level, a problem they share with many other nuclear EDFs. Still, in most cases the parametrizations with low $a_{\rm surf}$ value are much closer to experiment than those with large $a_{\rm surf}$.

(vii) For the majority of cases that we have studied, the SLy5sX parametrizations give very similar values for the quadrupole deformations of a given normal-deformed or superdeformed minimum in the energy surface. Differences are on the few percent level. In many cases, a SLy5sX parametrization with smaller $a_{\rm surf}$ gives slightly higher β_{20} than a parametrization with higher $a_{\rm surf}$, but that is clearly not a general rule. In any event, the differences between the parametrizations for quadrupole deformations are rarely significant. In most cases these values also agree very well with data from electromagnetic transition matrix elements in the yrast bands built on the deformed configuration in question. Similarly, predictions for higher multipole deformations with even ℓ are very similar for the majority of cases.

(viii) The situation is quite different for nuclei in regions where octupole deformation, either axial or nonaxial, plays a role for the ground state. The octupole deformation of the minimum becomes significantly more pronounced when reducing $a_{\rm surf}$, which also tends to improve agreement with (indirect) experimental data. In turn, in some cases such minima can disappear completely when using a parametrization with large $a_{\rm surf}$. The available data for octupole deformed nuclei also show a clear preference for parametrizations with low $a_{\rm surf}$. Remaining deviations, however, indicate that there is also need for improvement of other properties of the nuclear EDF, most importantly details of shell structure that is at the origin of these minima.

It is important to note that all time-even terms in the EDF contribute to $a_{\rm surf}$, not just the gradient terms. As a consequence, in EDF-based methods $a_{\rm surf}$ is intertwined with the properties of infinite nuclear matter and shell structure. This has to be contrasted with macroscopic-microscopic approaches, where these three aspects of the model can be independently adjusted. For the SLy5sX parametrizations, the total size of all contributions to $a_{\rm surf}$ change when going from one parametrization to another:

(i) The terms in the EDF that contribute to the energy per particle of infinite nuclear matter contribute to about half the total value of $a_{\rm surf}$. As a consequence, the self-consistency of the protocol for parameter adjustment strongly correlates $a_{\rm surf}$ with $a_{\rm vol}$ and $a_{\rm sym}$. This correlation is such that the gross properties of two-neutron and two-proton separation energies are the same for all the SLy5sX parametrizations, in spite of their quite different symmetry energy coefficients.

(ii) Because of a sizable contribution from the spin-orbit interaction to $a_{\rm surf}$, which also has the opposite sign of the other large contributions, spin-orbit splittings of the SLy5sX parametrizations are correlated to $a_{\rm surf}$. This has some visible impact on shell structure, in particular the position of high-j intruder levels and the amplitude of the variation of shell effects in the deformation energy surfaces.

We note in passing that we did not find any significant correlation between the density profile of spherical nuclei obtained with the SLy5sX parametrizations and the value of their $a_{\rm surf}$.

The construction of the SLy5sX parametrizations [8] is part of ongoing efforts to improve the fit protocol of nuclear EDFs. The new element that we have thoroughly studied concerns the control of the deformation properties of EDFs. It confirms that superdeformed states and fission barriers are, as expected, sensitive to the fine-tuning of the surface energy coefficient.

At the mean-field level of modeling, results for highly deformed states obtained with SLy5s1 are clearly superior to those obtained with the majority of other Skyrme parametrizations [8,13], which have usually been adjusted without any regard to the surface energy. Compared to earlier widely used parametrizations of the Skyrme EDF that reach similar quality for highly deformed states, as SkM* [10], UNEDF1 [16], and UNEDF2 [17], SLy5s1 has several advantages. It performs much better for isotopic and isotonic trends of binding energies than SkM* (compare, for example, Fig. 17 with results presented in Ref. [83]), whose deficiencies in that respect were already pointed out in the original paper [10]. Also, unlike the UNEDF1 and UNEDF2 parametrizations that only define the time-even terms in the functional, SLy5s1 can be used without ambiguities to calculate time-odd terms in situations where time-reversal symmetry is broken, such as the calculation of odd- and odd-odd nuclei or the calculation of rotational bands. Therefore, SLy5s1 will be our parametrization of choice for future studies of the properties of heavy nuclei.

The full set of SLy5sX parametrizations can also be used for further studies of correlations between the surface energy coefficient and other properties of nuclei not addressed here. It presents the opportunity to complement studies of correlations between observables in finite nuclei and properties of infinite nuclear matter that can be carried out with the SV-based parametrizations of Ref. [119] or the SAMi-based parametrizations of Refs. [120,121]. Indeed, only families of fits that systematically vary a single property of the EDF allow for controllable correlation analyses.

The results presented here suggest that a simultaneous adjustment of the surface and surface symmetry energy coefficients will be needed for further improvement. They also show, however, that it is not sufficient to fine-tune only the surface energy. A better control of shell effects, which are at the origin of deformed minima, is equally important, in particular for the description of states with exotic shapes. The deficiencies of nuclear EDFs for single-particle spectra also concern many other observables. Earlier studies, however, indicate that it is unlikely that they can be systematically resolved within the current form of nuclear EDFs [17,81].

One has to note that the value of a_{surf} is not model independent. Its extraction from an EDF depends on the model that will be used to calculate nuclei [8]. Therefore, its "best value" as defined here is valid for parametrizations designed for mean-field calculations. It has to be redefined if correlations beyond mean field are introduced, such as corrections for spurious rotational motion or mixing of mean-field configurations. The same dependence on the model can be expected for the surface symmetry energy coefficient a_{ssym}. A comparison of several frequently used procedures for its calculation is presently underway [29], with the goal of finding a computationally friendly way to constrain it during parameter fits.

ACKNOWLEDGMENTS

We thank J. Bartel for an illuminating discussion on the construction of the SkM* parametrization. This work was supported by the French Centre national de la recherche scientifique (CNRS) through PICS Grant No. 6949, the University of Jyväskylä within the FIDIPRO program, and the IAP Belgium Science Policy (Brix network P7/12). The computations were performed using HPC resources from the Consortium des Équipements de Calcul Intensif (CÉCI), funded by the Fonds de la Recherche Scientifique de Belgique (F.R.S.-FNRS) under Grant No. 2.5020.11, and the CCIN2P3 of the CNRS.

[1] M. Bender, P.-H. Heenen, and P.-G. Reinhard, Self-consistent mean-field models for nuclear structure, Rev. Mod. Phys. **75**, 121 (2003).

[2] S. G. Nilsson and I. Ragnarsson, *Shapes and Shells in Nuclear Structure* (Cambridge University Press, Cambridge, England, 1995).

[3] M. Brack, J. Damgård, A. S. Jensen, H.-C. Pauli, V. M. Strutinsky, and C. Y. Wong, Funny hills: The shell-correction approach to nuclear shell effects and its applications to the fission process, Rev. Mod. Phys. **44**, 320 (1972).

[4] M. Brack and P. Quentin, Self-consistent average density matrices and the Strutinsky energy theorem, Phys. Lett. B **56**, 421 (1975).

[5] M. Brack and P. Quentin, The Strutinsky method and its foundation from the Hartree-Fock-Bogoliubov approximation at finite temperature, Nucl. Phys. A **361**, 35 (1981).

[6] P.-G. Reinhard, M. Bender, W. Nazarewicz, and T. Vertse, From finite nuclei to the nuclear liquid drop: Leptodermous expansion based on self-consistent mean-field theory, Phys. Rev. C **73**, 014309 (2006).

[7] J. Dobaczewski, W. Nazarewicz, and P.-G. Reinhard, Error estimates of theoretical models: A guide, J. Phys. G **41**, 074001 (2014).

[8] R. Jodon, M. Bender, K. Bennaceur, and J. Meyer, Constraining the surface properties of effective Skyrme interactions, Phys. Rev. C **94**, 024335 (2016).

[9] R. Jodon, Constraints on the nuclear energy density functional and new possible analytical forms, Ph.D. thesis, Université Lyon, 2014.

[10] J. Bartel, P. Quentin, M. Brack, C. Guet, and H.-B. Håkansson, Towards a better parametrization of Skyrme-like effective forces: A critical study of the SkM force, Nucl. Phys. A **386**, 79 (1982).

[11] M. Bender, K. Rutz, P.-G. Reinhard, and J. A. Maruhn, Consequences of the center-of-mass correction in nuclear mean-field models, Eur. Phys. J. A **7**, 467 (1999).

[12] M. Bender, P.-H. Heenen, and P. Bonche, Microscopic study of ^{240}Pu: Mean-field and beyond, Phys. Rev. C **70**, 054304 (2004).

[13] N. Nikolov, N. Schunck, W. Nazarewicz, M. Bender, and J. Pei, Surface symmetry energy of nuclear energy density functionals, Phys. Rev. C **83**, 034305 (2011).

[14] A. Pastore, D. Davesne, K. Bennaceur, J. Meyer, and V. Hellemans, Fitting Skyrme functionals using linear response theory, Phys. Scr. **T154**, 014014 (2013).

[15] M. Kortelainen, T. Lesinski, J. Moré, W. Nazarewicz, J. Sarich, N. Schunck, M. V. Stoitsov, and S. Wild, Nuclear energy density optimization, Phys. Rev. C **82**, 024313 (2010).

[16] M. Kortelainen, J. McDonnell, W. Nazarewicz, P.-G. Reinhard, J. Sarich, N. Schunck, M. V. Stoitsov, and S. M. Wild, Nuclear energy density optimization: Large deformations, Phys. Rev. C **85**, 024304 (2012).

[17] M. Kortelainen, J. McDonnell, W. Nazarewicz, E. Olsen, P.-G. Reinhard, J. Sarich, N. Schunck, S. M. Wild, D. Davesne, J. Erler, and A. Pastore, Nuclear energy density optimization: Shell structure, Phys. Rev. C **89**, 054314 (2014).

[18] J. F. Berger, M. Girod, and D. Gogny, Constrained Hartree-Fock and beyond, Nucl. Phys. **502**, 85 (1989).

[19] E. Chabanat, P. Bonche, P. Haensel, J. Meyer, and R. Schaeffer, A Skyrme parametrization from subnuclear to neutron star densities. Part II. Nuclei far from stabilities, Nucl. Phys. A **635**, 231 (1998) [Erratum: **643**, 441 (1998)].

[20] M. Bender, K. Bennaceur, T. Duguet, P.-H. Heenen, T. Lesinski, and J. Meyer, Tensor part of the Skyrme energy density functional. II: Deformation properties of magic and semi-magic nuclei, Phys. Rev. C **80**, 064302 (2009).

[21] V. Hellemans, P.-H. Heenen, and M. Bender, Tensor part of the Skyrme energy density functional. III. Time-odd terms at high spin, Phys. Rev. C **85**, 014326 (2012).

[22] W. Ryssens, V. Hellemans, M. Bender, and P.-H. Heenen, Solution of the Skyrme-HF+BCS equations on a 3D mesh, II: a new version of the EV8 code, Comput. Phys. Commun. **187**, 175 (2015).

[23] Y. M. Engel, D. M. Brink, K. Goeke, S. Krieger, and D. Vautherin, Time-dependent Hartree-Fock theory with Skyrme's interaction, Nucl. Phys. A **249**, 215 (1975).

[24] N. Schunck, J. Dobaczewski, J. McDonnell, J. Moré, W. Nazarewicz, J. Sarich, and M. V. Stoitsov, One-quasiparticle states in the nuclear energy density functional theory, Phys. Rev. C **81**, 024316 (2010).

[25] K. Pototzky, J. Erler, P.-G. Reinhard, and V. Nesterenko, Properties of odd nuclei and the impact of time-odd mean fields: A systematic Skyrme-Hartree-Fock analysis, Eur. Phys. J. A **46**, 299 (2010).

[26] A. Pastore, D. Tarpanov, D. Davesne, and J. Navarro, Spurious finite-size instabilities in nuclear energy density functionals: Spin channel, Phys. Rev. C **92**, 024305 (2015).

[27] B. Gall, P. Bonche, J. Dobaczewski, H. Flocard, and P.-H. Heenen, Superdeformed rotational bands in the mercury region. A cranked Skyrme-Hartree-Fock-Bogoliubov study, Z. Phys. A **348**, 183 (1994).

[28] C. Rigollet, P. Bonche, H. Flocard, and P.-H. Heenen, Microscopic study of the properties of identical bands in the $A = 150$ mass region, Phys. Rev. C **59**, 3120 (1999).

[29] J. Meyer *et al.* (unpublished).

[30] R. W. Hasse and W. D. Myers, *Geometrical Relationships of Macroscopic Nuclear Physics* (Springer-Verlag, Berlin, 1988).

[31] W. D. Myers and K.-H. Schmidt, An update on droplet-model charge distributions, Nucl. Phys. A **410**, 61 (1983).

[32] D. N. Poenaru, R. A. Gherghescu, and W. Greiner, Fissility of nuclear and atomic cluster systems, Rom. Rep. Phys. **63**, 1133 (2011).

[33] G. A. Leander and Y. S. Chen, Reflection-asymmetric rotor model of odd $A \sim 219 - 229$ nuclei, Phys. Rev. C **37**, 2744 (1988).

[34] H. J. Wollersheim *et al.*, Coulomb excitation of ^{226}Ra, Nucl. Phys. A **556**, 261 (1993); note that the objects called β_ℓ in this reference correspond to our $\alpha_{\ell 0}$ of Eq. (10).

[35] J. O. Denschlag, Nuclear Fission, in *Handbook of Nuclear Chemistry*, edited by A. Vértes, S. Nagy, Z. Klencsár, R. G. Lovas, and F. Rösch (Springer, Boston, 2011), p. 223.

[36] N. Bohr and J. A. Wheeler, The Mechanism of Nuclear Fission, Phys. Rev. **56**, 426 (1939).

[37] L. Liao and R. J. A. Hill, Shapes and Fissility of Highly Charged and Rapidly Rotating Levitated Liquid Drops, Phys. Rev. Lett. **119**, 114501 (2017).

[38] W. Ryssens, Symmetry breaking in nuclear mean-field models, Ph.D. thesis, Université Libre de Bruxelles, 2016.

[39] W. Ryssens, M. Bender, and P.-H. Heenen, MOCCa code (unpublished).

[40] P. Bonche, H. Flocard, and P.-H. Heenen, Solution of the Skyrme HF + BCS equation on a 3D mesh, Comput. Phys. Commun. **171**, 49 (2005).

[41] D. Baye, and P.-H. Heenen, Generalised meshes for quantum mechanical problems, J. Phys. A **19**, 2041 (1986).

[42] D. Baye, The Lagrange-mesh method, Phys. Rep. **565**, 1 (2015).

[43] W. Ryssens, P.-H. Heenen, and M. Bender, Numerical accuracy of mean-field calculations in coordinate space, Phys. Rev. C **92**, 064318 (2015).

[44] S. Bjørnholm and J. E. Lynn, The double-humped fission barrier, Rev. Mod. Phys. **52**, 725 (1980).

[45] A. N. Andreyev, K. Nishio, and K.-H. Schmidt, Nuclear fission: a review of experimental advances and phenomenology, Rep. Prog. Phys. **81**, 016301 (2018).

[46] T. Bürvenich, M. Bender, J. A. Maruhn, and P.-G. Reinhard, Systematics of fission barriers in superheavy elements, Phys. Rev. C **69**, 014307 (2004).

[47] L. Bonneau, P. Quentin, and D. Samsœn, Fission barriers of heavy nuclei within a microscopic approach, Eur. Phys. J. A **21**, 391 (2004).

[48] W. Younes and D. Gogny, Microscopic calculation of ^{240}Pu scission with a finite-range effective force, Phys. Rev. C **80**, 054313 (2009).

[49] Z. P. Li, T. Nikšić, D. Vretenar, P. Ring, and J. Meng,, Relativistic energy density functionals: Low-energy collective states of ^{240}Pu and ^{166}Er, Phys. Rev. C **81**, 064321 (2010).

[50] H. Abusara, A. V. Afanasjev, and P. Ring, Fission barriers in covariant density functional theory: Extrapolation to superheavy nuclei, Phys. Rev. C **85**, 024314 (2012).

[51] N. Schunck, D. Duke, H. Carr, and A. Knoll, Description of induced nuclear fission with Skyrme energy functionals: Static potential energy surfaces and fission fragment properties, Phys. Rev. C **90**, 054305 (2014).

[52] K. Rutz, J. A. Maruhn, P.-G. Reinhard, and W. Greiner, Fission barriers and asymmetric ground states in the relativistic mean-field theory, Nucl. Phys. A **590**, 680 (1995).

[53] M. Samyn, S. Goriely, and J. M. Pearson, Further explorations of Skyrme-Hartree-Fock-Bogoliubov mass formulaes. V. Extension to fission barriers, Phys. Rev. C **72**, 044316 (2005).

[54] A. N. Andreyev *et al.*, New Type of Asymmetric Fission in Proton-Rich Nuclei, Phys. Rev. Lett. **105**, 252502 (2010).

[55] M. Veselský, A. N. Andreyev, S. Antalic, M. Huyse, P. Möller, K. Nishio, A. J. Sierk, P. Van Duppen, and M. Venhart,

Fission-barrier heights of neutron-deficient mecury nuclei, Phys. Rev. C **86**, 024308 (2012).
[56] T. Ichikawa, A. Iwamoto, P. Möller, and A. J. Sierk, Contrasting fission potential-energy structure of actinides and mercury isotopes, Phys. Rev. C **86**, 024610 (2012).
[57] M. Warda, A. Staszczak, and W. Nazarewicz, Fission modes of mercury isotopes, Phys. Rev. C **86**, 024601 (2012).
[58] J. D. McDonnell, W. Nazarewicz, J. A. Sheikh, A. Staszczak, and M. Warda, Excitation-energy dependence of fission in the mercury region, Phys. Rev. C **90**, 021302(R) (2014).
[59] N. Dubray and D. Regnier, Numerical search of discontinuities in self-consistent potential energy surfaces, Comput. Phys. Commun. **183**, 2035 (2012).
[60] C. E. Bemis, Jr. *et al.*, E2 and E4 Transition Moments and Equilibrium Deformations in the Actinide Nuclei, Phys. Rev. C **8**, 1466 (1973).
[61] W. Ryssens, P.-H. Heenen, and M. Bender, Symmetry unrestricted Skyrme mean-field study of heavy nuclei, PoS (BORMIO2016) 033.
[62] S. Sels *et al.*, Shape staggering of midshell mercury isotopes from in-source laser spectroscopy compared with density-functional-theory and Monte Carlo shell-model calculations, Phys. Rev. C **99**, 044306 (2019).
[63] R. Capote *et al.*, RIPL - Reference input parameter library for calculation of nuclear reactions and nuclear data evaluations, Nucl. Data Sheets **110**, 3107 (2009).
[64] A. Mamdouh, J. M. Pearson, M. Rayet, and F. Tondeur, Large-scale fission-barrier calculations with the ETFSI method, Nucl. Phys. A **644**, 389 (1998); [Erratum: **648**, 282 (1999)].
[65] M. Hunyadi *et al.*, Excited superdeformed $K^\pi = 0^+$ rotational bands in β-vibrational fission resonances of ^{240}Pu, Phys. Lett. B **505**, 27 (2001).
[66] K. Pomorski and J. Dudek, Nuclear liquid-drop model and surface-curvature effects, Phys. Rev. C **67**, 044316 (2003).
[67] D. Ackermann and Ch. Theisen, Nuclear structure features of very heavy and superheavy nuclei – tracing quantum mechanics towards the 'island of stability', Phys. Scr. **92**, 083002 (2017).
[68] Yu. T. Oganessian *et al.*, Production and Decay of the Heaviest Nuclei ^{293,294}117 and ^{294}118, Phys. Rev. Lett. **109**, 162501 (2012).
[69] A. Lopez-Martens, T. Lauritsen, S. Leoni, T. Døssing, T. L. Khoo, and S. Siem, Population and decay of superdeformed nuclei probed by discrete and quasi-continuum γ-ray spectroscopy, Prog. Nucl. Part. Phys. **89**, 137 (2016).
[70] T. L. Khoo *et al.*, Excitation Energies and Spins of a Superdeformed Band in ^{194}Hg from One-Step Discrete Decays to the Yrast Line, Phys. Rev. Lett. **76**, 1583 (1996).
[71] K. Hauschild *et al.*, Yrast superdeformed band in ^{194}Pb: J^π and E_x, Phys. Rev. C **55**, 2819 (1997).
[72] T. Lauritsen *et al.*, Experimental determination of the excitation energy of superdeformed bands in ^{192,194}Hg by analysis of the decay quasicontinuum γ rays, Phys. Rev. C **62**, 044316 (2000).
[73] A. N. Wilson *et al.*, Direct Decays from Superdeformed States in ^{192}Pb observed Using Time-Correlated γ-Ray Spectroscopy, Phys. Rev. Lett. **90**, 142501 (2003)
[74] A. N. Wilson *et al.*, Excitation Energies of Superdeformed States in ^{196}Pb: Towards a Systematic Study of the Second Well in Pb Isotopes, Phys. Rev. Lett. **95**, 182501 (2005).
[75] A. N. Wilson *et al.*, Two-Particle Separation Energy Trends in the Superdeformed Well, Phys. Rev. Lett. **104**, 162501 (2010).
[76] S. Takahara, N. Tajima, and N. Onishi, Study of superdeformation in non-rotating states using the Skyrme-Hartree-Fock method, Nucl. Phys. A **642**, 461 (1998).
[77] J. Yao, M. Bender, and P.-H. Heenen, Systematics of low-lying states of even-even nuclei in the neutron-deficient lead region from a beyond-mean-field calculation, Phys. Rev. C **87**, 034322 (2013).
[78] N. Bree *et al.*, Shape Coexistence in the Neutron-Deficient Even-Even $^{182-188}$Hg Isotopes Studied Via Coulomb Excitation, Phys. Rev. Lett. **112**, 162701 (2014).
[79] K. Wrzosek-Lipska *et al.*, Electromagnetic properties of low-lying states in neutron-deficient Hg isotopes: Coulomb excitation of ^{182}Hg, ^{184}Hg, ^{186}Hg, and ^{188}Hg (unpublished).
[80] B. Singh, R. Zywina, and R. B. Firestone, Table of superdeformed nuclear bands and fission isomers, Nucl. Data Sheets **97**, 241 (2002); note that the objects called β in Table 3 of this reference correspond to our α_{20} of Eq. (10).
[81] T. Lesinski, M. Bender, K. Bennaceur, T. Duguet, and J. Meyer, The tensor part of the Skyrme energy density functional. Spherical nuclei, Phys. Rev. C **76**, 014312 (2007).
[82] L. Bonneau, P. Quentin, and P. Möller, Global microscopic calculations of ground-state spins and parities for odd-mass nuclei, Phys. Rev. C **76**, 024320 (2007).
[83] P.-H. Heenen, J. Dobaczewski, W. Nazarewicz, P. Bonche, and T. L. Khoo, Shell effects in superdeformed minima, Phys. Rev. C **57**, 1719 (1998).
[84] M. Wang, G. Audi, F. G. Kondev, W. J. Huang, S. Naimi, and X. Xu, The AME2016 atomic mass evaluation (II). Tables, graphs and references, Chin. Phys. C **41**, 030003 (2017).
[85] M. Bender, G. F. Bertsch, and P.-H. Heenen, Collectivity-induced quenching of signatures for shell closures, Phys. Rev. C **78**, 054312 (2008).
[86] J. Dudek, Nuclear superdeformation at high spins, Prog. Part. Nucl. Phys. **28**, 131 (1992).
[87] J. Terasaki, P. H. Heenen, P. Bonche, J. Dobaczewski, and H. Flocard, Superdeformed rotational bands with density dependent pairing interactions, Nucl. Phys. A **593**, 1 (1995).
[88] A. N. Andreyev *et al.*, A triplet of differently shaped spin-zero states in the atomic nucleus ^{186}Pb, Nature (London) **405**, 430 (2000).
[89] M. Bender, P. Bonche, T. Duguet, and P.-H. Heenen, Configuration mixing of angular momentum projected self-consistent mean-field states for neutron-deficient Pb isotopes, Phys. Rev. C **69**, 064303 (2004).
[90] R. R. Rodríguez-Guzmán, J. L. Egido, and L. M. Robledo, Beyond mean field description of shape coexistence in neutron-deficient Pb isotopes, Phys. Rev. C **69**, 054319 (2004).
[91] T. Duguet, M. Bender, P. Bonche, and P.-H. Heenen, Shape Coexistence in ^{186}Pb: Beyond-mean-field description by configuration mixing of symmetry restored wave functions, Phys. Lett. B **559**, 201 (2003).
[92] E. Clément *et al.*, Shape coexistence in neutron-deficient krypton isotopes, Phys. Rev. C **75**, 054313 (2007).
[93] M. Girod, J.-P. Delaroche, A. Görgen, and A. Obertelli, The role of triaxiality for the coexistence and evolution of shapes in light krypton isotopes, Phys. Lett. B **676**, 39 (2009).
[94] T. R. Rodríguez, Structure of krypton isotopes calculated with symmetry-conserving configuration-mixing methods, Phys. Rev. C **90**, 034306 (2014).

[95] J. M. Yao, K. Hagino, Z. P. Li, J. Meng, and P. Ring, Microscopic benchmark study of triaxiality in low-lying states of ^{76}Kr, Phys. Rev. C **89**, 054306 (2014).
[96] N. Paul *et al.*, Are There Signatures of Harmonic Oscillator Shells Far from Stability? First Spectroscopy of ^{110}Zr, Phys. Rev. Lett. **118**, 032501 (2017).
[97] B. Bucher *et al.*, Direct Evidence of Octupole Deformation in Neutron-Rich ^{144}Ba, Phys. Rev. Lett. **116**, 112503 (2016).
[98] J. Dudek, A. Góźdź, N. Schunck, and M. Miśkiewicz, Nuclear Tetrahedral Symmetry: Possibly Present throughout the Periodic Table, Phys. Rev. Lett. **88**, 252502 (2002).
[99] P. A. Butler and W. Nazarewicz, Intrinsic reflection asymmetry in atomic nuclei, Rev. Mod. Phys. **68**, 349 (1996).
[100] P. A. Butler, Octupole collectivity in nuclei, J. Phys. G **43**, 073002 (2016).
[101] L. M. Robledo and G. F. Bertsch, Global systematics of octupole excitations in even-even nuclei, Phys. Rev. C **84**, 054302 (2011)
[102] R. N. Bernard, L. M. Robledo, and T. R. Rodríguez, Octupole correlations in the ^{144}Ba nucleus described with symmetry-conserving configuration-mixing calculations, Phys. Rev. C **93**, 061302(R) (2016).
[103] S. Raman, C. W. Nestor, Jr., and P. Tikkanen, Transition probability from the ground to the first-excited 2^+ state of even-even nuclides, At. Data Nucl. Data Tables **78**, 1 (2001).
[104] P. Schüler *et al.*, High-spin states in ^{224,226,228}Th and the systematics of octupole effects in even Th isotopes, Phys. Lett. B **174**, 241 (1986).
[105] W. Reviol *et al.*, Characterization of octupole-type structures in ^{221}Th, Phys. Rev. C **90**, 044318 (2014).
[106] J. F. C. Cocks *et al.*, Spectroscopy of Rn, Ra and Th isotopes using multi-nucleon transfer reactions, Nucl. Phys. A **645**, 61 (1999).
[107] W. Ryssens, M. Bender, and P.-H. Heenen (unpublished).
[108] F. K. McGowan, C. E. Semis, Jr. W. T. Milner, J. L. C. Ford, Jr., R. L. Robinson, and P. H. Stelson, Coulomb excitation of vibrational-like states in the even-A actinide nuclei, Phys. Rev. C **10**, 1146 (1974).
[109] S. E. Agbemava, A. V. Afanasjev, and P. Ring, Octupole deformation in the ground states of even-even nuclei: A global analysis within the covariant density functional theory, Phys. Rev. C **93**, 044304 (2016).
[110] K. Nomura, D. Vretenar, and B.-N. Lu, Microscopic analysis of the octupole phase transition in Th isotopes, Phys. Rev. C **88**, 021303(R) (2013).
[111] W. Ryssens, M. Bender, and P.-H. Heenen, Towards symmetry-unrestricted Skyrme-HFB in coordinate-space representation: the example of rotational bands of the octupole deformed nucleus ^{222}Th, Acta Phys. Pol. B **49**, 339 (2018).
[112] B.-N. Lu, J. Zhao, E.-G. Zhao, and S.-G. Zhou, Multidimensionally-constrained relativistic mean-field models and potential-energy surfaces of actinide nuclei, Phys. Rev. C **89**, 014323 (2014).
[113] N. Onishi and R. K. Sheline, The tetrahedral deformation in the nucleus ^{16}O, Nucl. Phys. A **165**, 180 (1971).
[114] J. Dudek, J. Dobaczewski, N. Dubray, A. Góźdź, V. Pangon, and N. Schunck, Nuclei with tetrahedral symmetry, Int. J. Mod. Phys. E **16**, 516 (2007).
[115] N. Schunck, J. Dudek, A. Góźdź, and P. H. Regan, Tetrahedral symmetry in ground and low-lying states of exotica A $\sim$ 110 nuclei, Phys. Rev. C **69**, 061305(R) (2004).
[116] K. Zberecki, P.-H. Heenen, and P. Magierski, Nuclear tetrahedral configurations at spin zero, Phys. Rev. C **79**, 014319 (2009).
[117] S. Tagami, Y. R. Shimizy, and J. Dudek, Tetrahedral symmetry in Zr nuclei: Calculations of low-energy excitations with Gogny interaction, J. Phys. G **42**, 015106 (2015).
[118] J. Zhao, B.-N. Lu, E.-G. Zhao, and S.-G. Zhou, Tetrahedral shapes of neutron-rich Zr isotopes from a multidimensionally constrained relativistic Hartree-Bogoliubov model, Phys. Rev. C **95**, 014320 (2017).
[119] P. Klüpfel, P.-G. Reinhard, T. J. Bürvenich, and J. A. Maruhn, Variations on a theme by Skyrme: A systematic study of adjustments of model parameters, Phys. Rev. C **79**, 034310 (2009).
[120] X. Roca-Maza, M. Brenna, B. K. Agrawal, P. F. Bortignon, G. Colò, Li-Gang Cao, N. Paar, and D. Vretenar, Giant quadrupole resonances in 208Pb, the nuclear symmetry energy, and the neutron skin thickness, Phys. Rev. C **87**, 034301 (2013).
[121] L.-G. Cao, X. Roca-Maza, G. Colò, and H. Sagawa, Constraints on the neutron skin and symmetry energy from the anti-analog giant dipole resonance in ^{208}Pb, Phys. Rev. C **92**, 064304 (2015).